NUNATARYUK

Grant Agreement number: 773421

H2020-BG-2016-2017/H2020-BG-2017-1

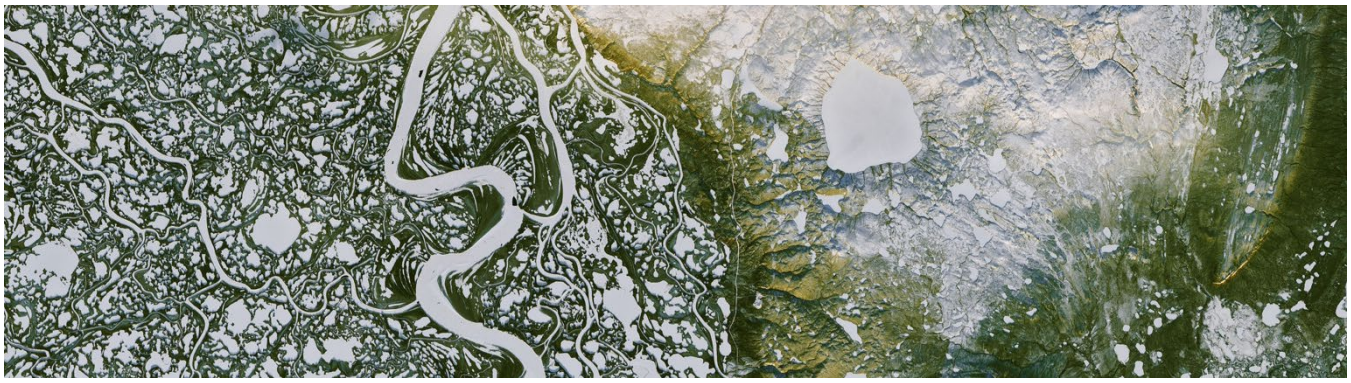

Deliverable Report

Please note, this report can be max. 52MB in size.

Work package	WP6
Deliverable No. (DX.X) - Title	D6.4 – Report on calibrated and validated numerical models to estimate site specific stability of coastal infrastructure in a changing climate with thawing permafrost
Lead Beneficiary (acronym)	NTNU/DTU
Lead Scientist responsible for the report (Name, Institution)	Seyed Ali Ghoreishian Amiri, NTNU Gustav Grimstad, NTNU Raed Lubbad, NTNU
Editors (Name, Institution)	Seyed Ali Ghoreishian Amiri, NTNU Gustav Grimstad, NTNU
Contributors (Name, Institution)	Knut V. Høyland, NTNU; Chuangxin Lyu, NTNU; Mohammad Akhsanul Islam, NTNU; Thomas Ingeman-Nielsen, DTU
Status	☒ Draft ☐ WP manager accepted ☐ Project coordinator accepted
Nature	R
Dissemination level	☒ PU - Public ☐ PP - Restricted to programme participants ☐ RE - Restricted to a group specified by the consortium ☐ CO - Confidential, only for members of the Consortium
Submission Date	28/10/2022

Summary

This report presents an overview of the costal erosion model and the infrastructure stability model that are capable of predicting the site-specific response to the global warming and thawing permafrost. The models are developed/modified during the NUNATARYUK project. This report is necessary because the increased Arctic coastal erosion together with permafrost degradation pose a significant threat to the communities living close to the coasts. It provides a brief description of the models, and their calibration procedures, and demonstrates a couple of validation case studies.

The costal erosion model described in this report is a comprehensive process-based model. It couples the thermodenudation and thermoabrasion processes with nearshore hydrodynamics and sediment transport. A couple of open-source packages are combined in this model with in-house models/codes to simulate the Arctic coastal erosion processes in a sequentially coupled manner. A simplified 1D storm surge module introduced by Dean and Dalrymple (1991), and the SWAN package developed at TU-Delft (TU-Delft, 2021) are employed to simulate the storm surge and wave generation in the offshore zone, respectively. The waves and related hydrodynamic forces together with sediment transport and morpho-dynamics are simulated using XBeach (*Deltares*, 2022). The processes related to permafrost melting and erosion of the bluffs are simulated with in-house modules implemented in XBeach. The model is calibrated and validated with field measurements from one of the Arctic coasts along the Kara Sea. The simulations confirms that the erosion mechanism is greatly influenced by the nearshore hydrodynamics and provide justification for including a hydrodynamic model to simulate Arctic coastal erosion.

The coastal infrastructure stability model in this report is a thermo-hydro-mechanical (THM) constitutive model that can represent the behaviour of frozen and unfrozen soil at the representative elementary volume (REV) scale, and in a unified manner. The presented model can describe the mechanical behaviour of frozen soil, including creep, as function of temperature, up to the unfrozen sate and vice versa. The model is designed for clay material, but the idea behind the model can be extended for sand as well. The model is implemented in Plaxis package, which is a software widely used by geotechnical engineers, and is capable of simulating the coupled THM behaviour of porous media, like clay deposits, at the global scale, using the finite element (FE) method. The calibration procedure is described in the report. All model parameters can be found using laboratory tests at the REV scale. The model is calibrated and validated using the field measurements conducted in the National Geo-test Site located at Longyearbyen Svalbard, and reasonable agreements have been achieved. It is also used to simulate the permafrost degradation and settlement of a footing with various embedment depth and applied stress for different imposed warming scenarios for the next 50 years. The simulations results confirm the importance of creep deformation for the serviceability and stability of infrastructures on warming permafrost, particularly in clay deposits.

Table of Contents

1 Introduction

Approximately one-third of the coast worldwide consists of permafrost, for which the average retreat rate is close to 0.5 meters per year (*Lantuit et al.*, 2011). For instance, in recent decades, coastal retreat along the Kara Sea has been measured between 1 and 1.7 metres per year (*Isaev et al.*, 2019). The annual maximum retreats along the Alaskan coast were approximately 22 metres for the years 2007 (*Jones et al.*, 2009). Many other Arctic coasts are retreating at the same level of magnitude. Observations along the various Arctic coasts have led to the establishment of a link between increased coastal erosion and warmer air temperature and increased permafrost temperature among the others.

Apart from coastal erosion, permafrost degradation has been observed as a result of global warming in the last half a century. This ongoing process arouses great concern on the infrastructure damage and is a threat to human safety on degrading permafrost. *Ramage et al.* (2021) estimated that around 3.3 million inhabitants, in the Arctic Circumpolar Permafrost Region, currently live in settlements where permafrost will ultimately disappear by 2050.

Increased Arctic coastal erosion together with permafrost degradation pose a significant threat to the communities living close to the coasts. Infrastructures along and close to the shores are compromised, heritage sites are at risk, and the lifestyle of the indigenous people is also affected. Moreover, within the next decade, the surface air temperature is expected to exceed the normal range of variability. Therefore, guidelines for infrastructure adaptation and human mitigation are necessary and should be determined by regional site investigations and engineering models.

The Nunataryuk project is a transdisciplinary research program focusing on the complex human-environmental interactions present along permafrost coastlines in the Arctic. By combining data gathering, research, and modelling, the program seeks to move to a more advanced characterization of the coastal permafrost environment of the Arctic. One focus of this research is to develop, calibrate and validate reliable models to predict the site-specific long-term variation of permafrost temperature in response to global warming scenarios and its consequences on the coastal erosions, and stability of infrastructures in the area.

2 Scope of the report

The modelling approach explained here after, and the models described in this report, will deal with phenomena associated with ground deformation and failure related to global warming and melting permafrost. They are expected to predict the variation of ground temperature in a long-term prospective and calculate the effects of this temperature variation on the coastal erosion, as well as stability of infrastructures around the coastal area. The top boundary of the models in this context is limited to ground surface, and the environmental loads including ground surface temperature are assumed to be known.

In general, the reliability of long-term predictions for the effects of climate change on the local coastlines and infrastructures depend to a very large extend on the reliability of the climate models that predict the regional variation in air temperature, based on the possible global emission scenarios in future. Climate models are quite complex models that should consider interactions with different natural and man-made CO_2 emission sources. Among the others, the interaction between air temperature and permafrost thawing is of high importance and goes both ways. As temperature rises, the ‘active layer’ deepens and permafrost thaws. The remains of long-frozen plants and animals in the permafrost also begin to thaw, and consequently, the organic material decomposes, emitting carbon dioxide, and methane when oxygen is not present. These greenhouse gases enter the atmosphere, which in turn will amplify the global warming. The climate modelling is out the scope of this report, and it is assumed that the available climate models and results reflect the effect of CO_2 emission scenarios on local air temperature.

The available predicted (or measured in case of validation) air temperature needs to be translated to ground surface temperature as the top thermal boundary condition of a ground or coast model. The difference between surface ground temperature and air temperature is correlated with factors such as surface radiation, vegetation and snow cover. Simplified and relatively advanced models are currently available in the literature to calculate the ground surface temperature from a given air temperature. Accuracy and reliability of these models are not in the scope of this report, and it is again assumed that the given ground surface temperature is reliable and can be considered as a valid boundary condition.

3 A process-based model for Arctic coastal erosion

The environmental changes due to the climate warming has been triggering significant coastal erosion in the Arctic. The number of open-sea days in the Arctic is increasing rapidly. The seawater temperature anomalies reached 5°C in the Arctic Ocean (*Steele et al.*, 2008). The frequency and intensity of storms during summer are increased and expected to increase even more. Active layer thickness inside the coastal bluffs is also increased, which in turn leads to slumping and, consequently, loss of mass along the Arctic coast. On the other hand, the sea ice extent is shrinking, which enables longer fetches to generate larger waves. A longer open sea season also increases erosion along the coast. As a result, Arctic coastal retreat has increased by a factor of two in the last few decades (*Jones et al.*, 2020). These phenomena show the effect of the nearshore hydrodynamics on Arctic coastal erosion, which is also justified through simulations conducted during the Nunataryuk project (see *Islam and Lubbad* (2022) for more details).

Aré (1988) describes two mechanisms that govern coastal bluff erosion in the Arctic: thermodenudation and thermoabrasion. In the thermodenudation process, melted permafrost during longer and warmer summers, leads to the slumping of the unfrozen bluffs by gravitational forces. The slumped materials are washed away from the beach by waves, tides and storm surges. Thermodenudation contributes slowly and continuously to retreating of the coast. In contrast, thermoabrasion is a rapid and episodic phenomenon. Thermoabrasion is triggered during summer storms when surges inundate the beach. This leads to forming the wave-cut niches at the bluff's base. The bluff will finally collapse when the growing niche becomes deep enough. The collapsed material degrades on the beach and eventually washes away under hydrodynamic forces. Aré's description shows the importance of the interactions between nearshore hydrodynamics, thermal process, and mechanics in modelling coastal erosion phenomena in the Artic. As it is also shown by *Islam and Lubbad* (2022), a generic model for Arctic coastal erosion should include these coupled interactions.

This section briefly describes a comprehensive process-based model that couples the thermodenudation (dominated by thermal processes) and thermoabrasion (mechanically driven) processes with nearshore hydrodynamics and sediment transport. More details of the model can be found in (*Islam and Lubbad*, 2022). Different open-source packages are coupled with in-house models/codes to simulate the above-mentioned processes together. The waves and related hydrodynamic forces together with sediment transport and morpho-dynamics are simulated using XBeach (*Deltares*, 2022). Two-way coupling is established between (1) hydrodynamic forces and sediment transport in XBeach on the one hand and (2) mechanical and thermal erosion processes in an in-house model on the other hand.

3.1 Model description

As discussed, the root of Arctic coastal erosion is back to offshore where waves are generated and water level increases due to storms. Thus, the modelling domain begins in offshore, and the whole domain is divided into three zones, i.e., offshore, nearshore and beach bluffs (see *Figure 1*). As shown in the figure, offshore zone of the domain is bounded by BC1 and BC2. The simplified 1D storm surge module introduced by *Dean and Dalrymple* (1991), and the SWAN package (*TU-Delft*, 2021) are employed to simulate the storm surge and wave generation in the offshore zone, respectively. The SWAN and storm surge model are coupled with the XBeach package at

the BC2 boundary. The boundary BC2 is defined where the mean sea level (h_m) and wavelength (λ) have a ratio of less than 0.5. At the BC2, water level and wave conditions are specified based on SWAN and storm surge model results. The transformation of the wave, wave setup and set down, and morphological changes in the nearshore zone are simulated by XBeach. The processes related to permafrost melting and erosion of the bluffs are simulated with in-house modules and coupled with XBeach.

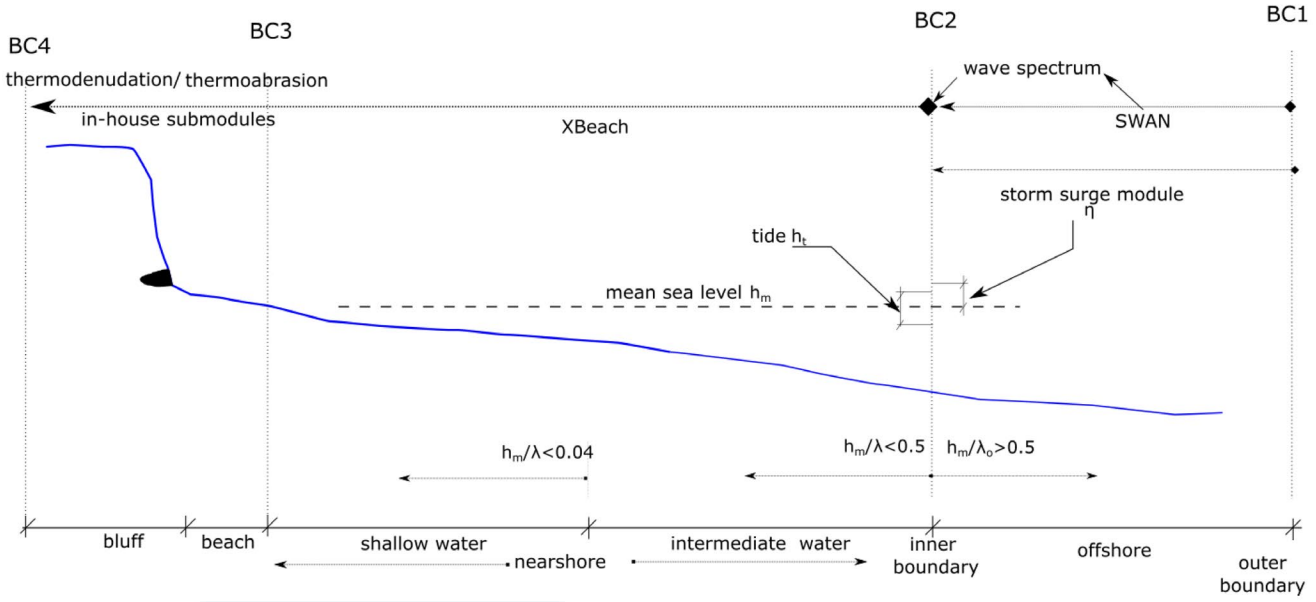

Figure 1 The spatial zones of the model are marked with four boundaries. Swan and storm surge modules calculate the hydrodynamics boundary conditions at BC2, which acts as input for xbeach. The outputs of xbeach are used as input for the submodules of thermodenudation and thermoabrasion (Islam and Lubbad, 2022)

3.1.1 Thermodenudation module

The thermodenudation module simulates thermally driven processes within the beach and bluff. It contains two submodules (namely: permafrost thaw; and slumping) to simulate the processes of permafrost melting and slumping at the bluff face.

3.1.1.1 Submodule: Permafrost thaw

The permafrost along the coastal profile can be divided into four sections: bluff surface; bluff face; beach; and seabed, as shown in Figure 2. The sections are defined based on the nature of the convective heat transfer into the bluff. The warm air and/or seawater bring the thermal energy necessary to thaw the permafrost inside the bluffs. In a simplified 1-dimensional model, the thawing rate (*m/s*) might be calculated as (*Ravens et al.*, 2017):

$$\dot{x}_t = \frac{h_{c_\alpha}(T_\alpha - T_s)}{L_t} \; ; \; \alpha = a, w \qquad (1)$$

where x_t is the thawing depth (assumed to be normal to the bluff surface), h_{c_α} is the convective heat transfer coefficient from air or water, T_α is the temperature of the water or air, T_s is the temperature of the seabed or bluff, and L_t is the latent heat of permafrost (energy per volume).

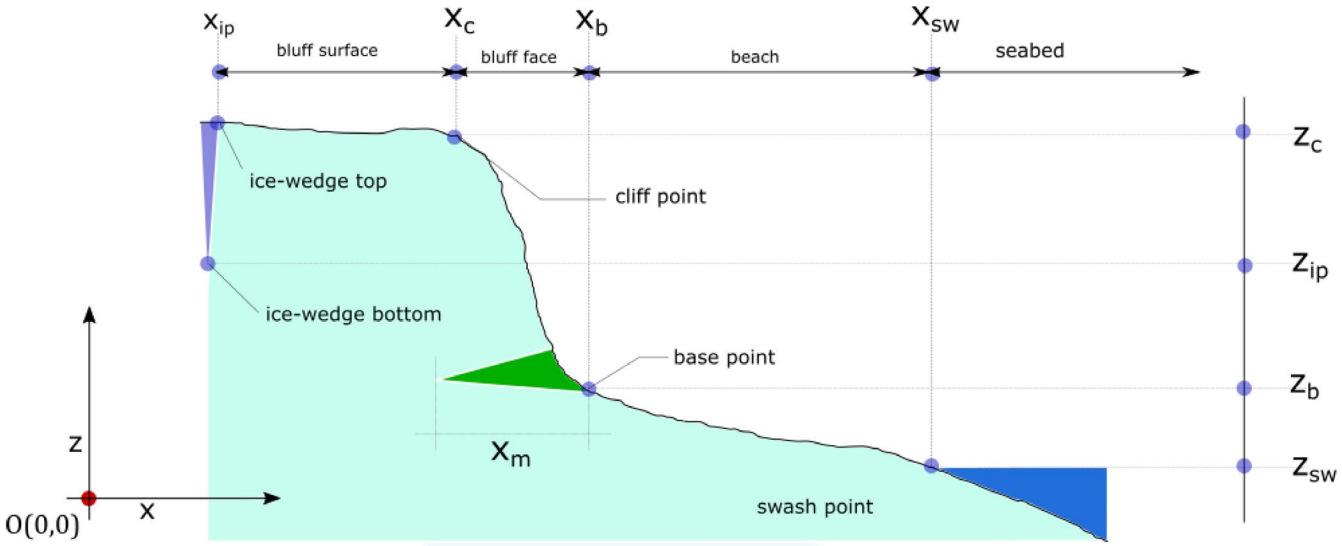

Figure 2 The coastal profile is divided into four sections based on the thermal energy transfer mechanisms. The most active portion in terms of thawing is the bluff face (Islam and Lubbad, 2022)

3.1.1.2 Submodule: Slumping

The thawed sediments at the bluff face fall due to gravitational forces and lack of strength in the thawed material when the slope of the bluff faces is quite steep. It should be noted, although the slope of the bluff face triggers slumping, the thawing rate, $\dot{x}_t$, is the key parameter controlling the mass fluxes to the beach by slumping. A critical slope on the bluff face, m_{cr}, is defined at which the thawed material will fall under the influence of gravity (see Figure 3). The following conditions must be fulfilled to trigger slumping:

$$\frac{dz}{dx} \geq \begin{cases} m_{cr;w} & \text{if } x_t > 0,\ h > 0.05 \text{ m} \\ m_{cr;a} & \text{if } x_t > 0,\ h < 0.05 \text{ m} \end{cases} \quad (2)$$

where $\frac{dz}{dx}$ is the slope of the coastal profile at a given point, $m_{cr;a}$ and $m_{cr;w}$ are the critical slopes for dry and wet conditions, respectively, and h is the mean water depth.

3.1.2 Thermoabrasion module

During the storm surges with a combined effect of waves (wave setup, wave run-up) and tide, the water reaches the base of the bluffs, and a niche starts to grow. This module simulates the niche growth, subsequent bluff collapse, and collapsed-bluff degradation in three submodules. The behaviour of the submodules is highly dependent on the boundary conditions, especially the water level at the base of the bluffs, h_{id}, and water temperature, T_w.

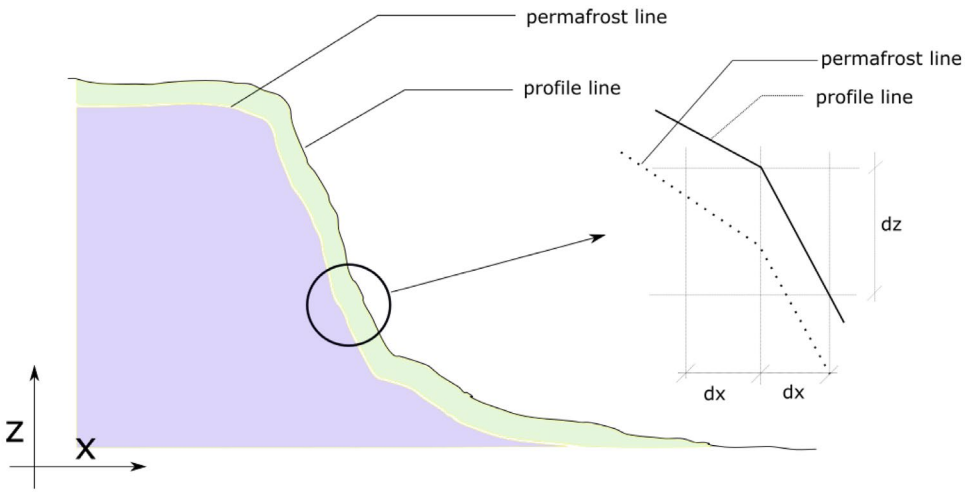

Figure 3 Slumping occurs when the thawed materials fall due to gravity. The triggering condition is: (1) thawing depth (x_t) is greater than zero, and (2) slope at the point (dz/dx) is greater than the critical slope (m_{cr}) (Islam and Lubbad, 2022)

3.1.2.1 Submodule: Niche growth

When the water level reaches the base of the bluff (point B in Figure 4), the warm water creates a niche. The geometry depicted in Figure 4 is adapted and simplified from the *Kobayashi* (1985) model.

The water depth at the base of the bluff; point B in the figure, termed h_{id}, is obtained from the results of XBeach simulation. The melting face, line EE', is vertical and assumed to be βh_{id}, where β is an empirical parameter. The value of β is taken as 2.0 according to *Ravens et al.* (2012). The niche depth, line $BE' = x_m$, is estimated from the following equation:

$$x_m = 2\varsigma_m\sqrt{\xi t} \tag{3}$$

where ξ and ς_m are the surf zone diffusivity, and a salinity adjustment, respectively:

$$\xi = Ah_{id}\sqrt{gh_{id}} \tag{4}$$

$$\varsigma_m = 0.0094(T_w - T_m) \tag{5}$$

where h_{id} is the time-averaged depth of water at the base of the bluff, g is the gravitational acceleration, A is an empirical constant taken as 0.4 according to *Longuet-Higgins* (1970), T_w is the temperature of the seawater, and T_m is the salinity adjusted melting point of the ice.

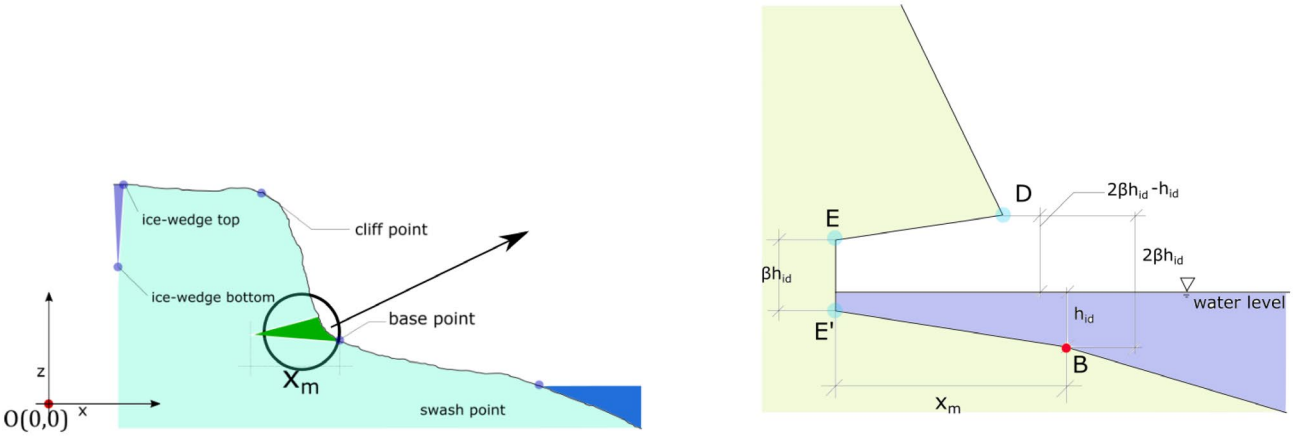

Figure 4 Niche geometry during the storm surge; simplified from Kobayashi (1985) by Islam and Lubbad (2022)

3.1.2.2 Submodule: Bluff collapse

The wave-cut niche at the base of the bluff creates instability, which may lead to the collapse of the bluffs. A critical combination of the various geometrical parameters, such as niche opening, niche depth, the position of ice-wedge polygon and the mechanical strength parameters, such as internal friction and cohesion, leads to the collapse of the bluffs. The location of the failure line/plane may vary according to the various combinations of the parameters. Two principal modes are identified for bluff collapse: (1) shear failure and (2) overturning failure. Shear failures are related to the mechanical strength of the bluffs. Figure 5 shows a possible shear failure mode. The shaded region over the niche, in Figure 5-a, is susceptible to collapse. The failure line, in this case, is GE, and the shaded region by the geometry GCDE is collapsed. A generalised and simplified condition of shear failure of the bluff is described by *Hoque and Pollard* (2009):

$$c.T_{ib} + W\cos\alpha.\tan\phi < W\sin\alpha \qquad (6)$$

where α is the angle of inclination of the failure plane, ϕ is the internal friction angle of the bluffs, T_{ib} is the tensile failure line of the bluff, c is cohesion, and W is the weight of the collapsed bluff (weight of the GCDE portion in the Figure 5-a).

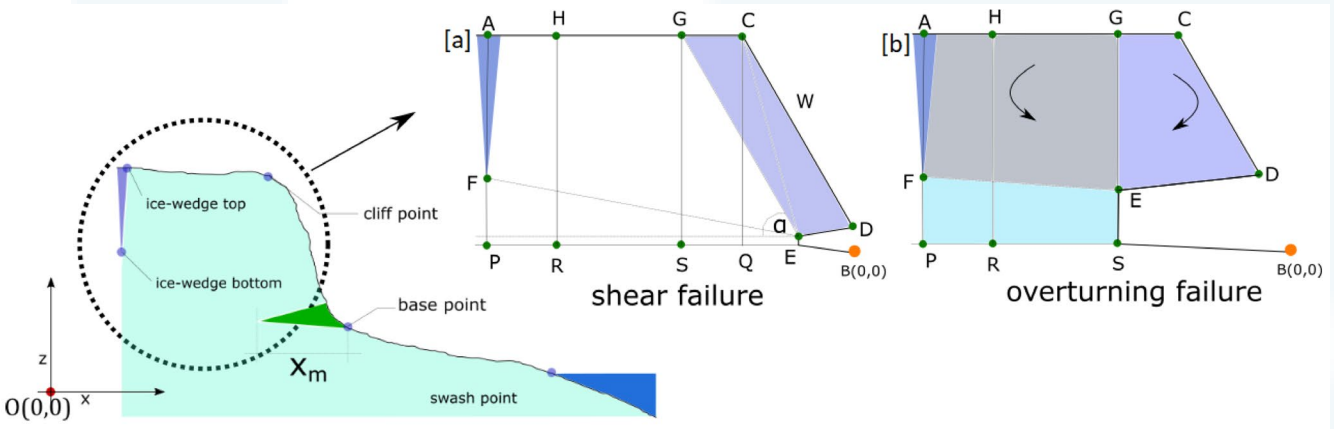

Figure 5 Two common failure modes of bluff collapse. [a] Shear failure of the bluffs, described by Eq. (6) [b] Overturning failure of the bluff described by Eq. (7) (Islam and Lubbad, 2022)

In the overturning failure mode, failure is initiated by the moment created by the overhanging portion of the bluff. The overturning occurs at the melting phase of the niche at point E in Figure 5-b. The shaded overhanging portion (GCDE) creates the driving moment in favour of the collapse, which is countered by the moment created by the remaining portion of the bluff (AHGEF). A small contribution comes from the friction along failure line EF and line AF. The failure mode is generalized by the following equation (simplified from the models by *Hoque and Pollard* (2009) and *Barnhart et al.* (2014)):

$$\tau_d > \tau_r + cT_{HF} + c_{ice}T_{VF} \quad (7)$$

where τ_d is the moment created by the overhanging bluff at the turning point, τ_r is the opposite moment created by the rest of the bluff, c is the cohesive strength of the bluff, T_{HF} is the horizontal failure line (line FE in the Figure 5-b), and T_{VF} is the vertical failure (line AF).

3.1.2.3 Submodule: Degradation of collapsed bluffs

The collapsed bluff stays on the beach and degrades over time. The degradation rate of the bluff can be estimated from the following equation (*Ravens et al.*, 2012):

$$M_i = M_{i-1}\left(1 - H^n\left[T_w - T_m\right]\right) \quad (8)$$

where M is the remained mass of the collapsed bluff at the end of timestep i and $i-1$, T_w is the seawater temperature, T_m is the salinity adjusted melting point of ice, H is the significant wave height at the 3 meters water depth, and a and n are empirical parameters, which according to *Ravens et al.* (2012) are taken as 800 kg/m-°C and 1.47, respectively.

3.2 Model calibration

Some of the input parameters of the model, such as critical slope (m_{cr}), convective heat transfer coefficient (h_{c_α}), water level (wl), and tensile strength of permafrost (c) are site-specific and should be calibrated based on the field investigations conducted on a specific study site. The calibration procedure is therefore explained in this section according to the field investigations have been conducted on one of the Arctic coasts, Baydaratskya Bay in the Kara Sea, since the summer of 2012. The study area is in the north-east region of Russia. The study area is quite large, and thus only two zones of it, namely S#1 and S#2, are selected for demonstration in this report. One profile from each zone (P#1 in S#1 and P#8 in S#2) are selected for calibration. More details of the site investigations, the study area and the zones can be found in *Islam and Lubbad* (2022).

3.2.1 Methodology of calibration

The convective heat transfer coefficient of the permafrost thaw module has to be calibrated against measurements of the thawing depth (x_t). The thawing depth at the bluff surface is estimated from the temperature measurements at the calibration profile. The remaining parameters of the model are calibrated by iterations to find the combinations that yield the closest estimate of the erosion volume. For the iterations, the initial values and upper/lower limits for the different parameters are assessed based on theoretical estimates and site observations.

The morphological changes in the coastal profile from the shoreline to the bluffs must also be considered in the calibration. The calibration process should intend to simulate the morphological changes at the bluffs and the beaches as close as possible to the measurements. The indicators of erosion measurements, such as (a) crest retreat, (b) erosion volume, and (c) the slope of the bluff face, are the targets. Out of the three erosion indicators, the primary target is to simulate erosion by volume, i.e., the volumetric changes between the calculation of two consecutive years with minimum deviation from measurements.

3.2.2 The Baydaratskya Bay case-study

A continuous time series of thawing depth for a bluff surface at a calibration profile is shown in Figure 6 for the summer of 2017. The thawing depth of this profile is simulated using the permafrost thaw module through a trial-and-error procedure around the convective heat transfer coefficient (h_{c_a}) to reach the best fit. The calibration result for $h_{c_a} = 106$ *W/m²-K* is also shown in Figure 6.

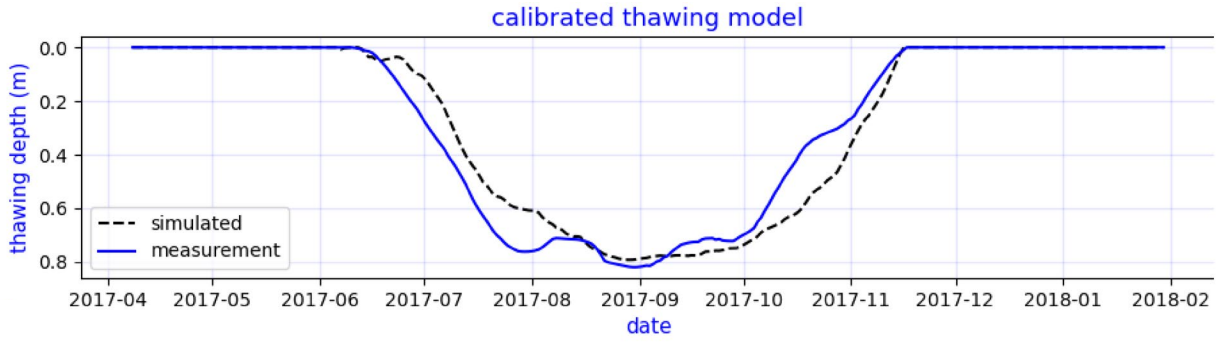

Figure 6 The thawing depth measurement and simulation by the thawing module (Islam and Lubbad, 2022)

As mentioned earlier, the convective heat transfer coefficient is different for the four sections shown in Figure 2, i.e. bluff surface, bluff face, beach and seabed. In this site, the temperature profile was not recorded for the bluff surface, the beach and the seabed. So, these three values have to be calibrated using trials and errors to match the total erosion volume. However, as a starting point and guidance, upper and lower limiting values might be considered. Following the model from *Kobayashi et al.* (1999), h_{c_w} (the value for water) will be limited to values between 500-800 *W/m²-K*. For h_{c_a} of bluff slope and dry portion of the beach, the initial value of iterations can be determined by the equation for the forced convection of a turbulent flow over a flat plate:

$$N_u = \frac{h_c.L}{k_f} = 0.037\,\mathrm{Re}^{0.8}\,\mathrm{Pr}^{1/3} \tag{9}$$

where N_u is the Nusselt number, k_f is the thermal conductivity of the fluid, L is the characteristic length, Re is the Reynolds number, and Pr is the Prandtl number. Using $\mathrm{Pr} = 0.71$ for air, the initial value of h_{c_a} is estimated to be approximately 25 *W/m²-K*.

The water level (wl) at boundary BC2 (see Figure 1) has to be updated at each timestep. It is estimated by superimposing water level changes due to tide (h_t) and storm surge (η) on the mean sea level (h_m). At the BC2 boundary, the water level is treated as the boundary condition for the XBeach, expressed by the following equation:

$$wl(t) = h_t(t) + \eta(t) + h_m \tag{10}$$

where h_m stands for the mean sea level, which is constant during the simulation (not a function of time), h_t is the water level changes due to tide at three-hour intervals (interpolated from the measurement), and η is the storm surge level estimated at three-hour intervals by the storm surge submodule. For calibration, the field measurements of sea level are used with the Russian State Geodetic Coordinate System (GSK-2011). It is also used as a datum for the numerical model. The values of h_t and η are not subject to calibration. The upper and lower limits of wl are the constraints imposed from field observations: (1) the water level does not touch the base of the bluffs during high tide on a calm day (upper limit of wl) and (2) the length of the beach from the base of bluffs to the swash zone varies from 40 to 70 meters (lower limit of wl).

The slumping process inside the numerical model is controlled and triggered using one single parameter: the critical slope (m_{cr}). The initial values for the trials are estimated from the field measurements of the coastal profiles. The bluff height and bluff slope of 30 measurements are shown in Figure 7. The coastal profiles shown in the figure are the observations that were free of snow at the time of measurements. These measurements were taken between 2012 to 2017 on several profiles of S#1 and S#2. The slope of the profiles varies from 0.1 to 1.1. A distinct difference is visible between the bluff slopes of zones S#1 and S#2. The coastal profiles are measured at the end of the summer when the thermodenudation for the summer is almost complete. It is inferred that the slopes of the bluff faces are near-stable slopes, and thus, the critical slope should be more than these measured slopes.

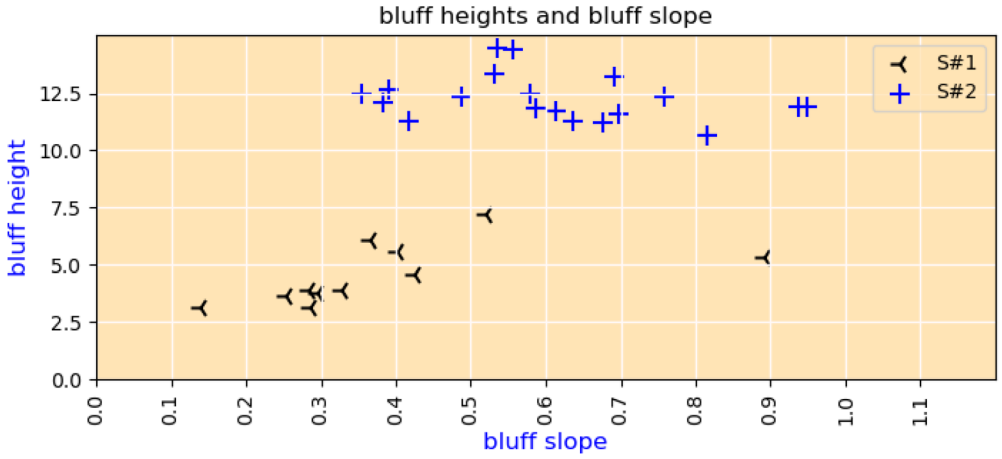

Figure 7 The relation of the bluff height and bluff slope in the study zones (Islam and Lubbad, 2022)

3.2.2.1 Calibration results

A trial-and-error procedure was made by applying the environmental forces (detailed in *Islam and Lubbad* (2022)) to find the combination of the parameters that yield the closest estimate of the erosion volume as the first target, and crest retreat, and the slope of the bluff face as the secondary targets. A summary of the calibrated values of the parameters is shown in Table 1, and a summary of the calibration results with the error measurements is shown in Table 2.

The simulated erosion volume for case#1 (P#1 in S#1; 15-09-2015 to 14-09-2016) and case#2 (P#8 in S#2; 15-09-2015 to 14-09-2016) differ from the measurements by 17.9% and 18.3% respectively (Figure 8 and Figure 9). Thermoabrasion (*ta*) is the dominating mechanism, contributing 75.78% of cumulative erosion volume, whereas, for case#2, thermoabrasion (*ta*) is 59.18%. Four collapses are simulated for case#1, but for case#2, two collapses are triggered within the model.

The sediment influx by thermodenudation is nearly three times greater for case#2 compared with case#1. Since the water level (wl) is the same for both cases, one can deduce that the higher sediment influx by thermodenudation changes the nearshore morphology and affects the rate of thermoabrasion.

The two collapses in case#2 are in sync with storms. Case#1 has two more additional collapses at the beginning of summer. The largest storm surge occurred during May, which did not result in any collapse, since the temperature of the water was not warm enough to rapidly grow the niche.

One of the secondary targets of the calibration procedure is to match the crest retreat of the bluffs. The crest retreat of the Arctic coast is retrogressive, i.e., always retreating as there is no restoration mechanism like the dune systems of the sandy beaches of warmer climates. The crest of the bluff is always moving towards the land.

The annual crest retreat rate is important for predicting vulnerability and associated risks. For case #1 and #2, the crest retreat was, respectively, 4.1 and 2.9 meters, according to the field observations. The model predicts crest retreats of 3.9 and 4 meters for case#1 and case#2, respectively. The results are shown in Figure 10.

Table 1 Summary of the calibrated parameters (Islam and Lubbad, 2022)

parameter	zone	symbol	calibrated value	unit	remarks
convective heat transfer coefficient	S#1 & S#2	h_{c_a}	106	W/m^2-k	for bluff-surface
	S#1 & S#2	h_{c_a}	98	W/m^2-k	for bluff-slope
	S#1 & S#2	h_{c_a}	90	W/m^2-k	for beaches
convective heat transfer coefficient	S#1 & S#2	h_{c_w}	700	W/m^2-k	for sea beds
Tensile strength	S#1 & S#2	τ	1xe7	N/m	
critical slope (dry)	S#1	m_{cr}	0.34	-	
	S#2	m_{cr}	0.52	-	
critical slope (wet)	S#1	m_{cr}	0.2	-	
	S#2	m_{cr}	0.2	-	
mean sea level	S#1 & S#2	h_m	-7.6	m	

Table 2 Summary of the calibration of case#1 and case#2 (td=thermodenudation and ta=thermoabrasion) (Islam and Lubbad, 2022)

case	criteria	measured	simulation				error (%)
				volume	(%)	net	
case#1	erosion volume ($m^3/m-width$)	7.04	td	2.01	24.22%	8.3	17.9%
			ta	6.29	75.78%		
	crest retreat (m)	4.1	-	-	-	3.9	4.8%
case#2	erosion volume ($m^3/m-width$)	12.51	td	6.04	40.82%	14.8	18.3%
			ta	8.75	59.18%		
	crest retreat (m)	2.9	-	-	-	4	37.9%

Another secondary target of the calibration is to match the shape (slope) of the profile at the bluff face and the elevation of the beach. The elevation of the beach is crucial since it affects the inundation depth (h_{id}), which in turn controls the thermoabrasion. The calibration result for case#1 is shown in Figure 11. It is observed that the simulation predicted a slope slightly steeper than the measurement. The predicted elevation of the beach was close to the measurements, albeit it overestimated the erosion by sediment transportation. The deviation is highest near the base of the bluff; errors near the beach are negligible. The model overestimates the erosion at the base of the bluffs. For case#2, shown in Figure 12, the model simulates the slope as much as the prediction. The simulated values deviated near the cliff points and the bluff base. The prediction at the beach was close.

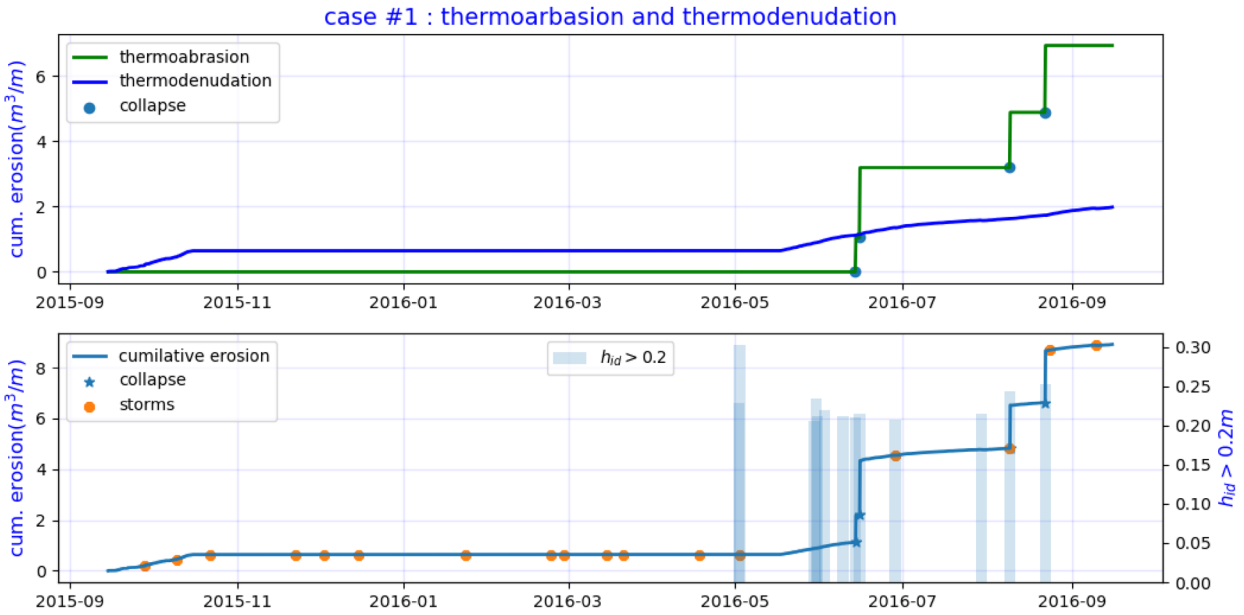

Figure 8 Results of the calibrated model of Case#1. Cumulative thermoabrasion and thermodenudation are shown separately. The sudden jumps in the erosion volumes indicate a bluff collapse by thermoabrasion. The erosion volume from the measurement was 7.04 m³/m-width, whereas the model simulated erosion of 8.3 m³/m-width. Thermodenudation contributes 2.01 out of 8.3 m³/m-width. Four collapses are simulated, and thermoabrasion contributes 75.7% of the erosion (Islam and Lubbad, 2022)

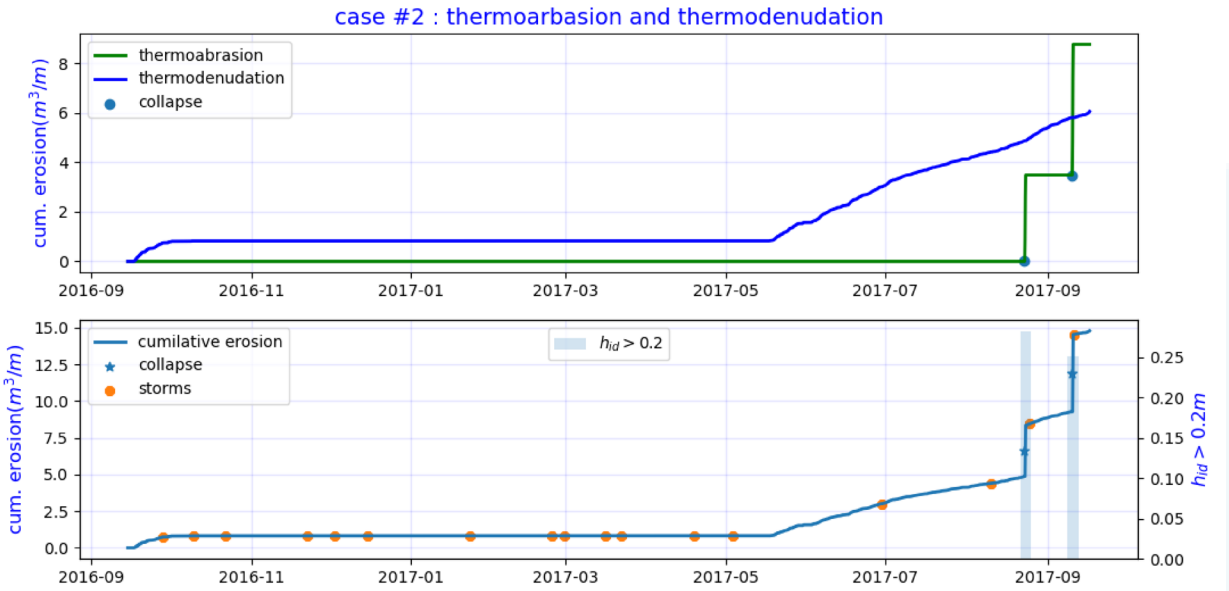

Figure 9 Results of the calibrated model of Case#2. The erosion volume from the measurement was 12.51 m³/m-width, whereas the model simulated erosion of 14.8 m³/m-width. Thermodenudation contributes 6.04 out of 14.8 m³/m-width; about three times greater than case#1. The bluff slope is steeper (0.9 vs 0.4) and the bluff height is higher (13 m vs 6 m). Two collapses are simulated and thermoabrasion contributes 59.18% of the erosion (Islam and Lubbad, 2022)

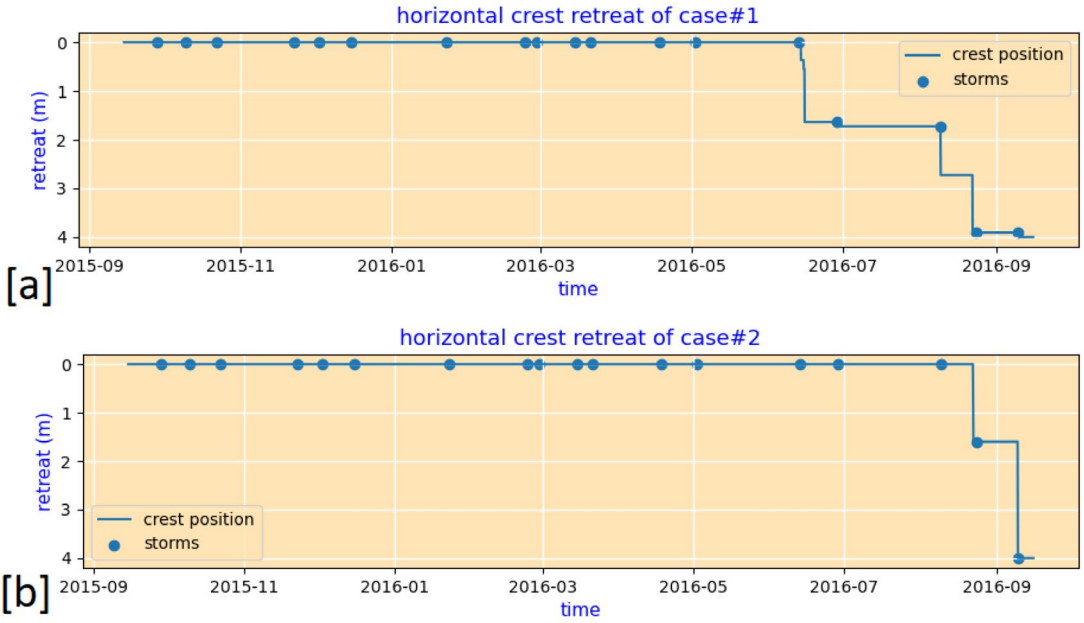

Figure 10 The crest retreat as a time series. The sudden drops are due to thermoabrasion, which contributed the most to the retreat (Islam and Lubbad, 2022)

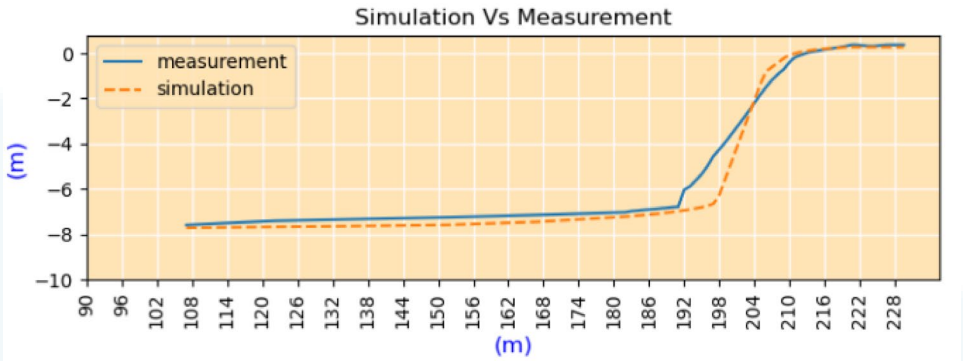

Figure 11 Case#1: prediction of the shape of the coastal profile after normalising the simulation around the middle of the bluff slope (Islam and Lubbad, 2022)

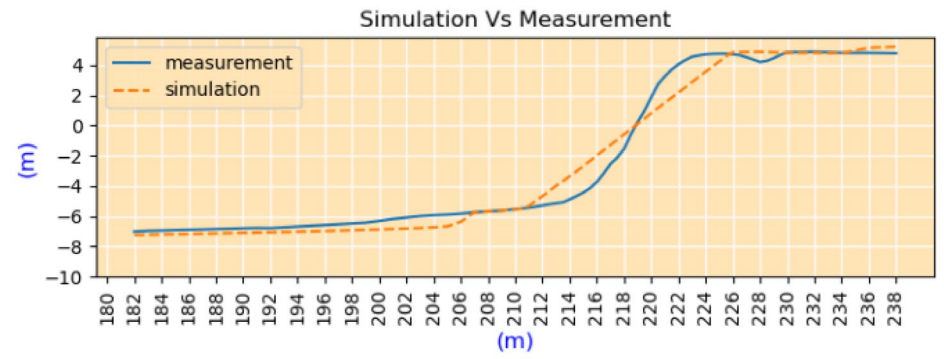

Figure 12 Case#2: prediction of the shape of the coastal profile after normalising the simulation around the middle of the bluff slope (Islam and Lubbad, 2022)

3.3 Model validation: The Baydaratskya Bay case-study

The calibrated model was applied to another three sets of measurements for validation. The new cases are summarized in Table 3. More details of the selected cases can be found in *Islam and Lubbad* (2022). Case#3 and case#4 are from profiles#1 and #8 for 2016-2017. Case#5 is from the two measurements of 2012 and 2017 on profile#1. Case#5 is selected to examine the performance of the numerical model for simulating long-term erosion.

Table 3 A summary of the three cases selected for the validation (Islam and Lubbad, 2022)

cases	zone	profile	Time		Crest retreat	Erosion	Accretion	Net Erosion
			From	To	(m)			$(m^3/m-width)$
case#3	S#1	P#1	15-09-2016	14-09-2017	3.2	28.73	0.00	28.73
case#4	S#2	P#8	15-09-2016	15-09-2017	3.9	11.81	0.00	11.81
case#5	S#1	P#1	13-06-2012	15-09-2017	16	71.05	0.00	71.05

The calibrated parameters shown in Table 2 are used for the validation cases without any changes. The time series of the environmental forces are updated and can be found in detail in *Islam and Lubbad* (2022). The initial thawing depths for case#3 and case#4 are used from the previous simulations (the thawing depth of the last timestep for case#1 and case#2). For case#5, the initial thawing depth was taken as zero because the case starts in June, not in September. From the thawing depth patterns of cases #1 and #2, we estimate that the thawing depth in June is zero.

The permafrost thawing module was calibrated with the measurements from summer of 2017, and validated using thawing depth measurements of summer 2014 from the same borehole. The thawing depth simulation mimics the field measurements (see Figure 13). The simulation could not capture the duration of thawing properly, but the depth is captured quite accurately.

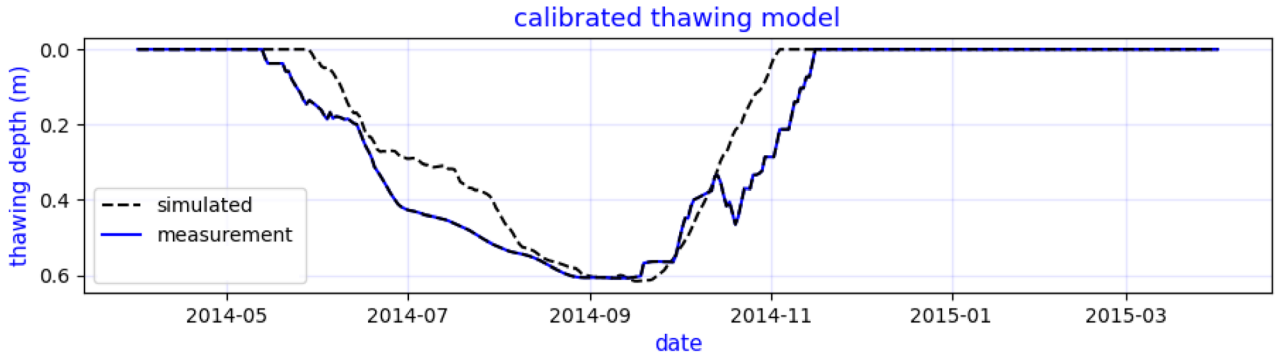

Figure 13 The erosion validation of the thawing module is completed using measurement of the summer of 2014 (Islam and Lubbad, 2022)

A summary of the overall results of the simulation for the selected cases is shown in Table 4 with the error measurements. The results show a good agreement with the measurements. The cumulative erosion volume simulated by the model for cases #3 to #5 are shown in Figure 14 to Figure 16, respectively.

Table 4 Summary of the validation cases (Islam and Lubbad, 2022)

case	criteria	measured	simulation				error (%)
				volume	(%)	net	
case#3	erosion volume ($m^3/m-width$)	28.73	td	10.18	39.46%	25.8	10.2%
			ta	15.62	60.54%		
	crest retreat (m)	3.2	-	-	-	3.9	4.8%
case#4	erosion volume ($m^3/m-width$)	11.81	td	3.75	24.83%	15.1	27.8%
			ta	11.36	75.17%		
	crest retreat (m)	3.9	-	-	-	-	23.1%
case#5	erosion volume ($m^3/m-width$)	71.05	td	23.6	29.32%	80.5	13.3%
			ta	56.9	70.68%		
	crest retreat (m)	16				14.8	7.5%

For case#3, the cumulative erosion of the profile reaches 25.8 *m³/m-width* which is slightly underestimated by the simulation. The erosion is dominated by thermoabrasion, but the contribution from thermodenudation increased from the previous year, from 24.3% to 33.22%. The rate of thermodenudation was higher during the summer of 2017. However, the prediction of the beach elevation deviated from the measurements. The shape of the bluff face was irregular, which the model failed to capture. Similar to the other cases, the deviation is higher near the base.

For case#4, the erosion is dominated by thermoabrasion (75.17%). The model estimated an erosion volume of 15.1 *m³/m-width,* which is overestimated from the measurement of 11.81 *m³/m-width*. Compared with case#2, case#4 demonstrated different behaviour. Thermoabrasion dominated the erosion mechanism with one initial big collapse.

The application of the model for the long-term erosion simulation is demonstrated by case#5. The simulation duration of this case is five years and four months. The erosion pattern of case#5 is similar to the other cases. The erosion is dominated by thermoabrasion (70.68%). The thermodenudation rate is different each year.

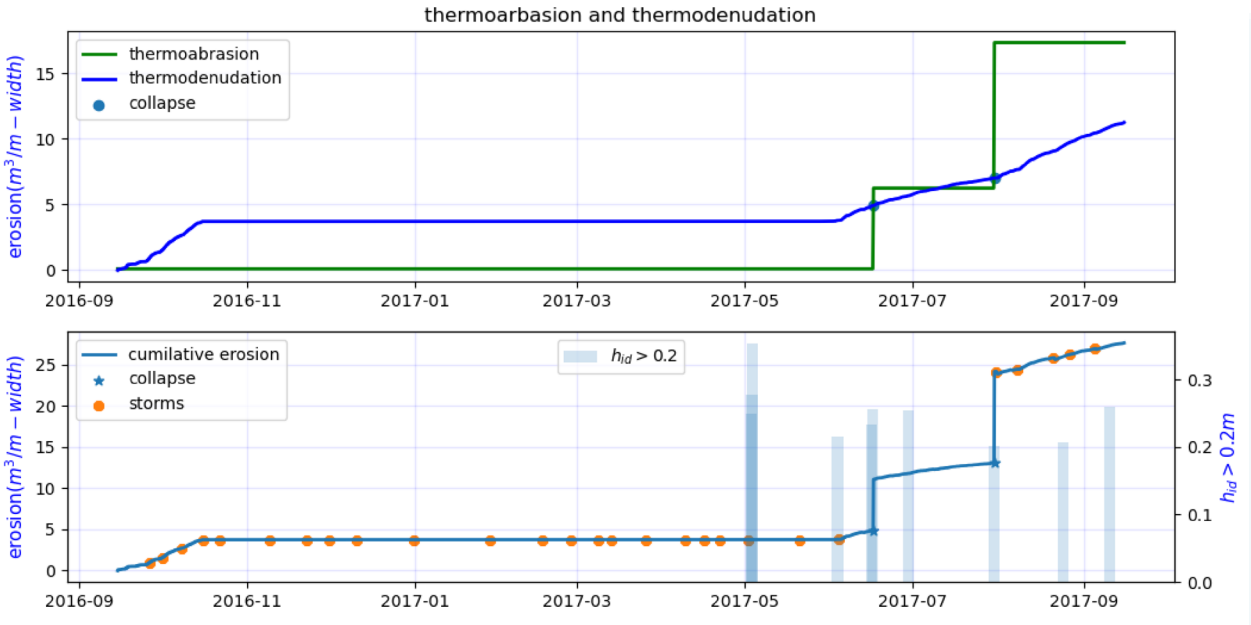

Figure 14 Erosion result for case#3 (Islam and Lubbad, 2022)

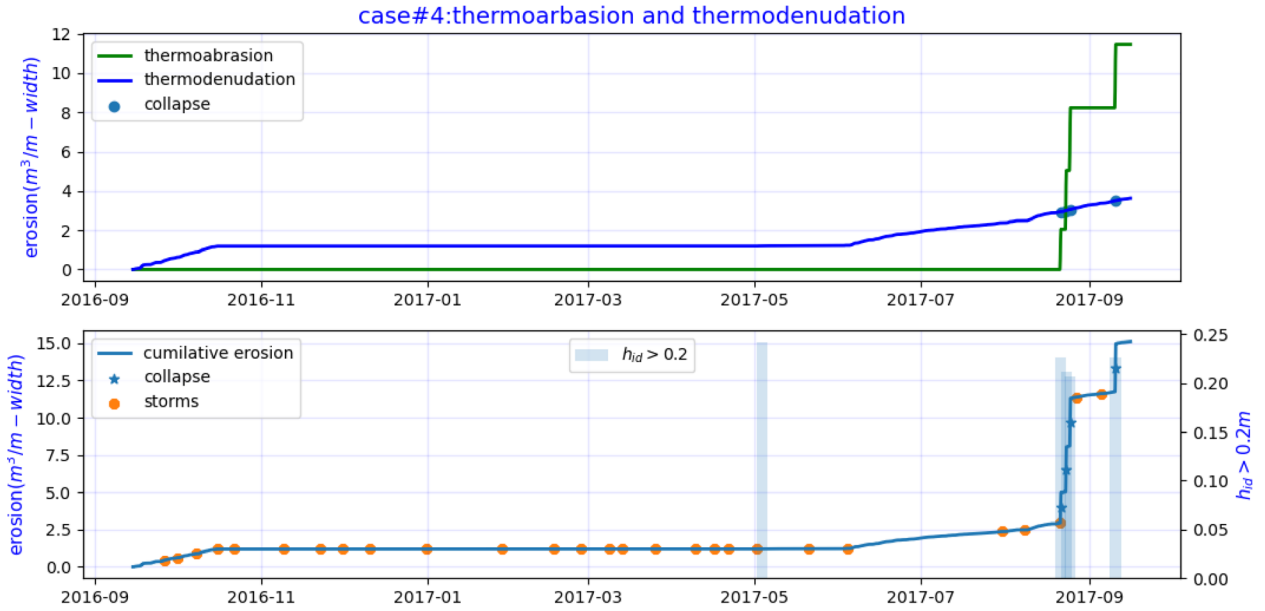

Figure 15 Erosion result for case#4

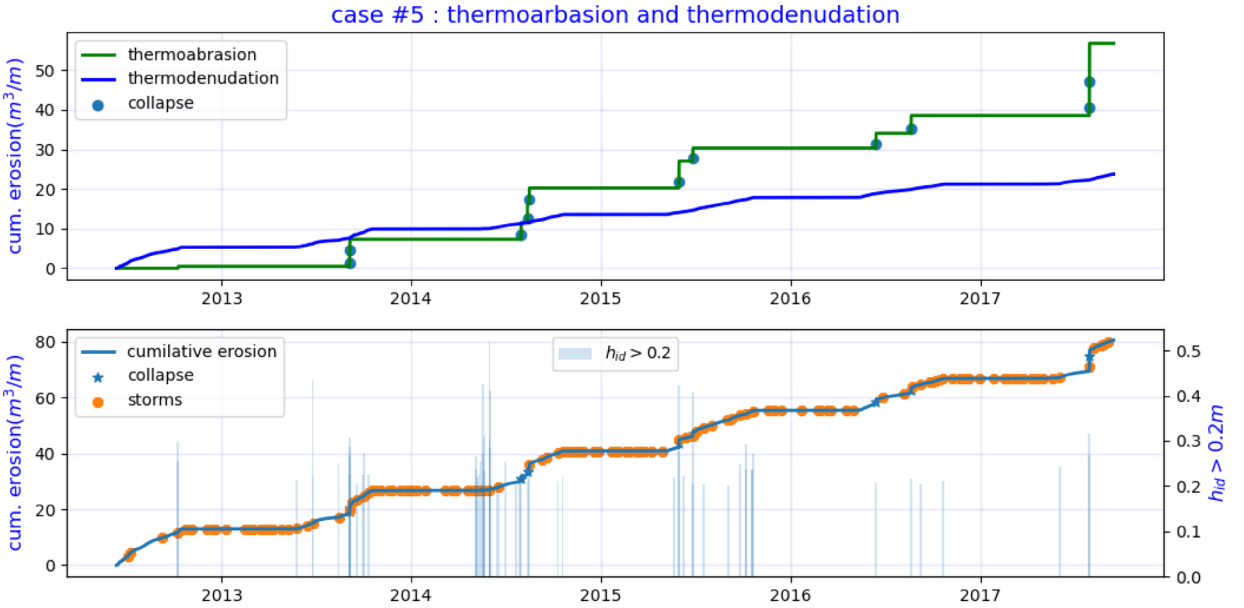

Figure 16 Erosion result for case#5

The deviation of the profile shape is shown in Figure 17. The deviation is higher at cliff points and bluff bases. During the five-year simulation, the beach elevation was simulated to be lower than the measurements; the deviation was nearly 0.3 metres, whereas the average deviation at the grid points was 0.86 metres.

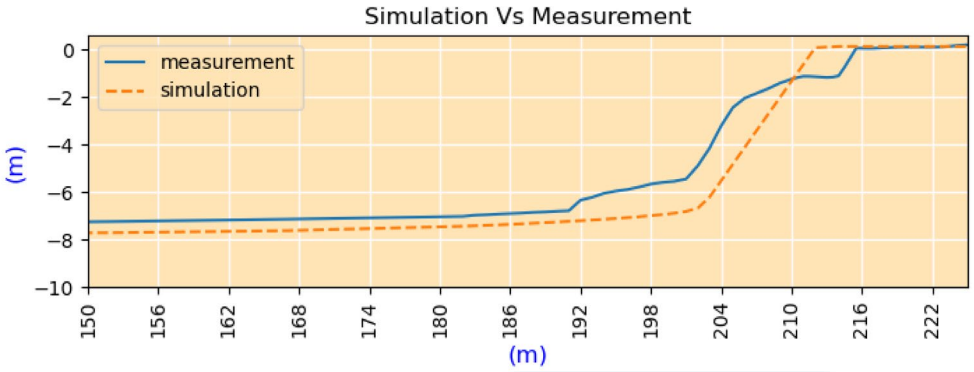

Figure 17 The shape of the profile after normalizing (Islam and Lubbad, 2022)

4 A constitutive model for infrastructure stability

The continuous warming trend observed in the Arctic since the 1980s creates concerns about the stability and durability of coastal infrastructure in permafrost regions. The increasing permafrost temperature will reduce the bearing capacity and increase settlement rates and subsidence of foundations. The active layer thickness is one the key parameters controlling the bearing capacity, but settlement rate might be highly affected, especially in clay deposits, by variation of ground temperature even in a range below the thawing temperature. This is related to consolidation and creep phenomena in clay material.

Clay in its partially frozen state may contain a considerable amount of unfrozen water, particularly at the sub-zero temperature close to the thawing temperature. Moreover, the hydraulic conductivity of warm frozen clay is relatively considerable, and thus, the dissipation of the excess unfrozen water could be an important factor that results in the settlement of frozen clay deposits (i.e. consolidation). On the other hand, considering the viscous nature of behaviour in many clay materials (which results in creep deformation), the frozen clay deposits are expected to exhibit more creep deformation, as the pore ice in the clay matrix is a highly viscous material, particularly around the thawing temperature.

Current stability calculations are commonly performed through thermal analyses, focusing on the variation of active layer thickness, and omitting the effect of additional deformation due to consolidation and creep on the stability and serviceability of the infrastructures. Taking these factors in to account needs a comprehensive thermo-hydro-mechanical (THM) model that can handle the complex behaviour of the frozen soil at both global (soil mass) and local (representative elementary volume (REV)) scales.

Among the others, Plaxis software, as a package widely used by geotechnical engineers, simulates the coupled THM behaviour of porous materials, like clay, at the global scale, using the finite element (FE) method. However, to reach a reliable numerical simulation, a realistic constitutive model, which can represent the material behaviour at the REV scale, is needed to be implemented in the FE software. In the Nunataryuk project, Plaxis is selected as the simulation platform at the global scale, and a simplified version of the constitutive model introduce by *Ghoreishian Amiri et al.* (2022) is used to represent the mechanical behaviour of frozen clay.

This section briefly describes the above-mentioned constitutive model, its calibration procedure and demonstrates a validation example. More details of the model can be found in (*Ghoreishian Amiri and Grimstad*, 2017; *Ghoreishian Amiri et al.*, 2022; *Lyu*, 2021).

4.1 Model description

Saturated frozen soil is a natural particulate composite, composed of solid grains, ice and unfrozen water. The mechanical behaviour of frozen soils is strongly dependent on the content and temperature of the pore ice in the soil matrix. Considering ice crystals as a part of the solid phase, the following effective stress measure might be considered (*Ghoreishian Amiri et al.*, 2016):

$$\boldsymbol{\sigma}^{*} = \boldsymbol{\sigma} - s_w p_w \mathbf{I} \tag{11}$$

where $\boldsymbol{\sigma}^{*}$ is the solid phase stress, defined as the combined stress of soil grains and ice, s_w is the unfrozen water saturation (i.e. the ratio of the volume of unfrozen water on the volume of pores), and I denotes the unit tensor. Note that throughout this section, compressive stress and strain are assumed to be positive.

Ignoring the thermal expansion, and following the theory of small strain, any strain increment, $d\boldsymbol{\varepsilon}$, can be additively decomposed into the following parts:

$$d\boldsymbol{\varepsilon} = d\boldsymbol{\varepsilon}^{e} + d\boldsymbol{\varepsilon}^{vp} \tag{12}$$

where $d\boldsymbol{\varepsilon}^{e}$ and $d\boldsymbol{\varepsilon}^{vp}$ are the elastic and visco-plastic (inelastic) parts of strain, respectively.

The modified Cam-Clay (MCC) model, as the basic model representing the behaviour of clay at the unfrozen states, is considered here as the basis for further development to frozen states.

4.1.1 Elastic response

As mentioned, the material response in its frozen state depends on the content and temperature of the pore ice. Thus, the elastic parameters of the material should be modified accordingly. In this model, the common elastic parameters of the MCC model are evaluated separately at the fully unfrozen ($s_i = 0$) and frozen states ($s_i = s_{i\,\max}$), and being linearly interpolated based on the ice content at any arbitrary frozen state. On the other hand, the elastic parameter of ice is also temperature dependent, and needs to be modified. Assuming a linear dependency of elastic behaviour of ice with temperature, one can write the following equation for the Young's modulus:

$$E_f = E_{f_{ref}} - E_{f_{inc}}\left(T - T_{ref}\right) \tag{13}$$

where $E_{f_{ref}}$ is the value of E_f at the reference temperature (T_{ref}) and $E_{f_{inc}}$ denotes the rate of change in E_f with temperature. More detailed equations can be found in (*Ghoreishian Amiri et al.*, 2022).

4.1.2 Visco-plastic response

In the context of visco-plasticity, the common yield surface of plasticity theory is replaced by a convex set, that are associated with different strain rates, including the reference strain rate. The surface associated with the reference rate is known as the *reference surface*, and the one associated with the current strain rate is known as the *dynamic surface*. The dynamic surface always passes through the current stress sate and also keeps a similar shape to the reference surface with respect to a particular similarity centre. Thus, in terms of the MCC model, the elliptical yield surface of the MCC model, will be replaced by a set of ellipses with different sizes (i.e. different equivalent stresses), with a similarity centre at the origin of the stress space.

To reach a temperature dependent inelastic response, the size of the reference surface should be a function of temperature. This is done by introducing a temperature dependent equivalent stress for the reference surface:

$$p_{yr}^{*} = p_{c}^{*}\left(\frac{p_{y_{0r}}^{*}}{p_{c}^{*}}\right)^{\frac{\lambda_0-\kappa}{\lambda-\kappa}} \tag{14}$$

where

$$\lambda = \lambda_0\left[(1-r)\exp(-\beta S)+\mathrm{r}\right] \tag{15}$$

and p_c^* indicates the reference stress, $p_{y_{0r}}^*$ is the reference equivalent stress for the fully unfrozen state, κ denotes the compressibility coefficient of the system within the elastic region, λ_0 represents the compressibility coefficient for the unfrozen state along virgin loading, r is a constant related to the maximum stiffness of the soil, β is a parameter controlling the rate of change in soil stiffness with temperature, and S stands for cryogenic suction, which has a unique relation with temperature.

Due to the tensile strength of ice, frozen soils are expected to exhibit a tensile strength. The tensile strength of frozen soil will vary with temperature (or cryogenic suction). A linear relation between the tensile strength and cryogenic suction is assumed in this model.

The last modification of the MCC model is to alter the elliptical shape of the convex set to a function of ice content (or unfrozen water content). The shape modification must be done according to the fact that, in a fully frozen sate, when (almost) all of the liquid water turns to ice, the frozen clay will exhibit enormous compressive strength.

Applying all of these modifications to the MCC model, the resulted convex set will be of the form:

$$F = \left(p^{*}+p_t^{*}\right)\left[\left(p^{*}+p_t^{*}\right)s_w^{m}-\left(p_y^{*}+p_t^{*}\right)\right]+\left(\frac{q^{*}}{M}\right)^{2} \tag{16}$$

where p^* and q^* represent the mean and deviatoric parts of the solid phase stress, p_t^* and p_y^* stand for the tensile strength and equivalent stress; both are associated with the the current temperature of the soil and the strain rate, s_w is the unfrozen water content, M is the slope of the critical state line, and m is a constant parameter. The schematic shape of the convex set is presented in Figure 18. As shown in the figure, the convex set, at an unfrozen state, has elliptical shape, similar to the MCC model, while approaches to a sand-like model in a fully frozen state.

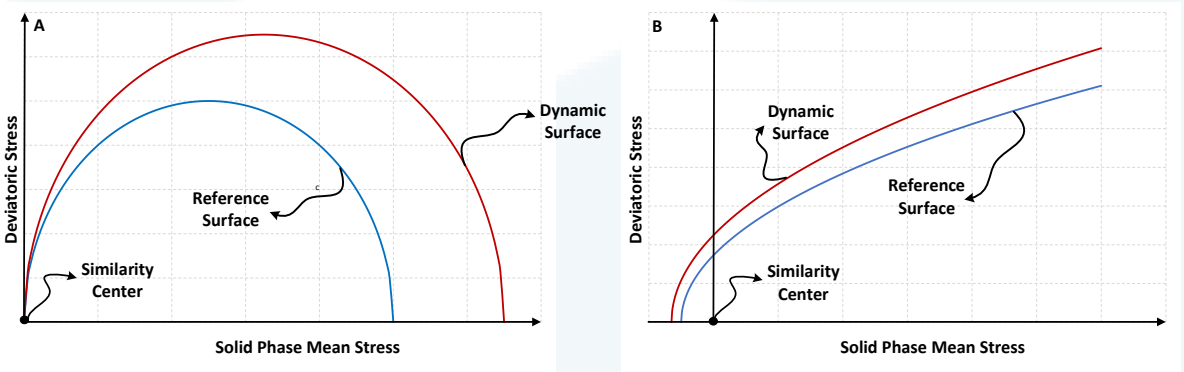

Figure 18 Reference and dynamic surfaces of the model for: A) unfrozen state; B) fully frozen state of the material with m=1 (Ghoreishian Amiri and Grimstad, 2017)

The incremental visco-plastic response can then be calculated as:

$$d\boldsymbol{\varepsilon}^{vp} = \mu_0\frac{\lambda_0(\lambda-k)}{\lambda(\lambda_0-k_0)}\left\langle R^{N}\right\rangle\frac{\partial Q}{\partial \boldsymbol{\sigma}^{*}}dt \tag{17}$$

where $\langle . \rangle$ is the Macaulay brackets, λ_0, λ, κ_0 and κ represent the elastic and elastoplastic compressibility of the system at the unfrozen and frozen states, respectively, μ_0 is the fluidity of the unfrozen soil at the reference strain rate, R is the similarity ratio of the dynamic and reference surfaces, N is creep number, dt is the time increment, and Q is the plastic potential surface, which is defined in this model as:

$$Q = s_w^{\gamma}\left[p^* - \frac{p_y^* + p_t^*}{2}\right]^2 + \left(\frac{q^*}{M}\right)^2 \tag{18}$$

The plastic potential surface specified the direction of the inelastic flow.

The last point is about the creep number. In common models for unfrozen soil the creep number is considered as constant parameters, while in frozen soils this assumption is not valid, as the rate dependency of frozen soils depends on the content and temperature of the pore ice. Thus, the following simple relation is assumed in this model:

$$N = N_0 + b_1 \times S - b_2 \times s_i \tag{19}$$

where N_0 is the creep number of the soil at a fully unfrozen state, S is cryogenic suction, s_i is the ice content, and b_1 and b_2 are two constant parameters.

More detailed formulation, like hardening rules and ice-bond breakage, can be found in (*Ghoreishian Amiri et al.*, 2022).

4.2 Model calibration

The model described in the previous section has been implemented in Plaxis, such that it can be used to perform a THM analysis to predict the site-specific long-term variation of permafrost temperature in response to global warming scenarios and its consequences on the stability of the infrastructures in the area. The full model requires fourteen mechanical parameters, four parameters regarding the rate dependency (creep deformation), three calibration parameters for the hydraulic behaviour and unfrozen water content, and two calibration parameters for heat flow. All parameters can be found using laboratory tests at the REV scale.

4.2.1 Thermo-hydraulic parameters

The unfrozen water content parameters are ideally calibrated with the soil freezing characteristic curve (SFCC). However, when SFCC is not available, one can alternatively use the soil water characteristic curve (SWCC) and the cryogenic suction (i.e. Clausius-Clapeyron equation) instead of the matric suction. It should be noted, this approach slightly underestimates the unfrozen water content (*Watanabe and Osada*, 2016).

The measurement of the hydraulic conductivity of frozen soils has been limited. Thus, hydraulic conductivity parameter(s) can be again estimated from unsaturated soils. According to *Watanabe and Osada* (2016) the hydraulic conductivity parameter(s) can be quite accurately calibrated by that of unsaturated unfrozen soil based on the unfrozen water content.

The relevant equations for hydraulic conductivity and SFCC models can be found in (*Lyu*, 2021).

Thermal properties (i.e. thermal conductivity and capacity) of frozen soil, as a complex mixture of solid grains, ice and unfrozen water, can be theoretically calculated based on the thermal conductivity of its constituents. The thermal properties of water and ice are quite known and is considered accordingly. The thermal conductivity of the solid grains can be determined and calibrated using a steady-state testing method. The schematic of the test setup is shown in Figure 19. By measuring the thermal properties of the frozen soil, the model can be calibrated

by tuning the thermal properties of the solid grains. More details about the testing procedure can be found in (*Lyu*, 2021).

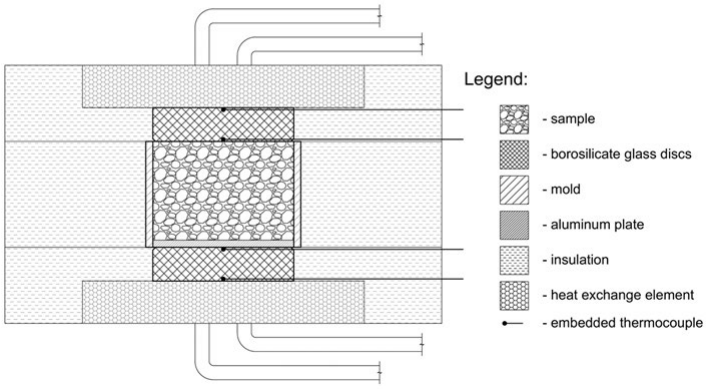

Figure 19 Cross-section of thermal conductivity test setup (Lyu, 2021)

4.2.2 Mechanical parameters including creep

Performing an isotropic drained compression test for an unfrozen state of the soil and plotting the results in the $\upsilon : \ln p^*$ plane (where υ is the specific volume) provide the data to find the elastic compressibility coefficient, κ_0, the reference stress, p_c^*, the initial value of the reference equivalent stress, $p_{y_{0r}}^*$, and the total compressibility coefficient, λ_0. Note that the parameters $p_{y_{0r}}^*$ and p_c^* should be determined at the reference strain rate.

A normal drained shear strength test at an unfrozen state of the soil provides the information needed to determine the elastic shear modulus of the soil in unfrozen state, G_0, and for the slope of the critical state line (M).

The information from a triaxial compression test in an arbitrary reference temperature at a frozen state of the soil, can be used for determining the reference Young's modulus of the frozen soil, $E_{f_{ref}}$. Similar test in a different negative temperature can be considered to find $E_{f_{inc}}$. Then, an isotropic compression test at a frozen state of the soil with a certain value of ice saturation can be used for calculating the Poisson's ratio of the soil in the fully frozen state, ν_f.

Considering Eq. (15), β and r can be calculated by determining λ at two different frozen states of the soil.

The viscous parameters for the unfrozen state of the soil, μ_0 and N_0, can be determined in a common way from oedometer tests at a constant strain rate or from a conventional oedometer test. Evaluating N in two different frozen states with certain values of cryogenic suction and ice content will provide required data to find b_1 and b_2. Then, the parameters γ, k_{t_1} and k_{t_2} can be determined using a trial-and-error procedure to fit the time to failure curves of the soil in two different frozen states.

4.3 Model validation: The Longyearbyen case study

Longyearbyen is the largest settlement in Svalbard, with around 2000 inhabitants. The permafrost at Svalbard is quite young, probably formed during and after the last ice age. Two benchmark sites are established in this area, for geotechnical testing and field investigation. Therefore, a systematic site investigation has been conducted since the year 2016 including soil characterization and monitoring of ground temperature profiles. A borehole down to 30 *m* depth was cased with 50 *mm* diameter plastic pipes, and instrumented with thermistor strings with 0.25~2 *m* depth spacing to achieve long-term continuous ground temperature measurement. The field

investigation indicates around 2 *m* active layer thickness and a stratigraphy with 3 meters sand layers (two layers of sand), and a homogeneous saline marine permafrost down to 30 *m*. More details on the characterization of the sites can be found in (*Gilbert et al.*, 2018; *Graham et al.*, 2019).

The Nunataryuk project in a collaboration with the Norwegian Geo Test Site (NGTS) project collected intact samples from these sites, for laboratory thermal, hydraulic, and mechanical testing. The details of the sampling method, testing procedures and results are found in (*Lyu*, 2021). Note that the focus of this study is on the clay deposit, so simple linear elastic behaviour is assumed for the sand layers. Their thermal properties are back calculated according to the field measurements. The calibrated parameters are summarized in Table 5. The calibration results in comparison with element test results are partly shown in Figures 20 and 21.

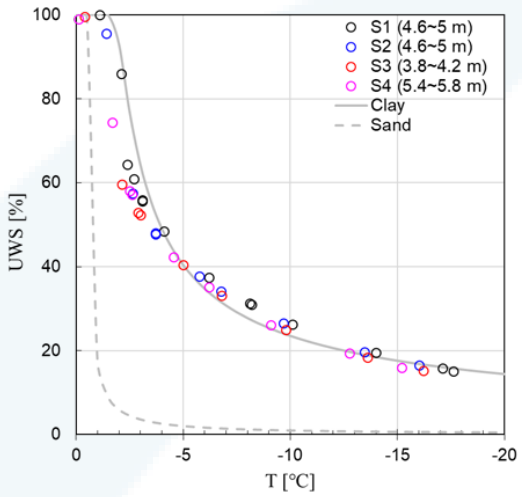

Figure 20 Unfrozen water saturation vs. temperature (Lyu, 2021)

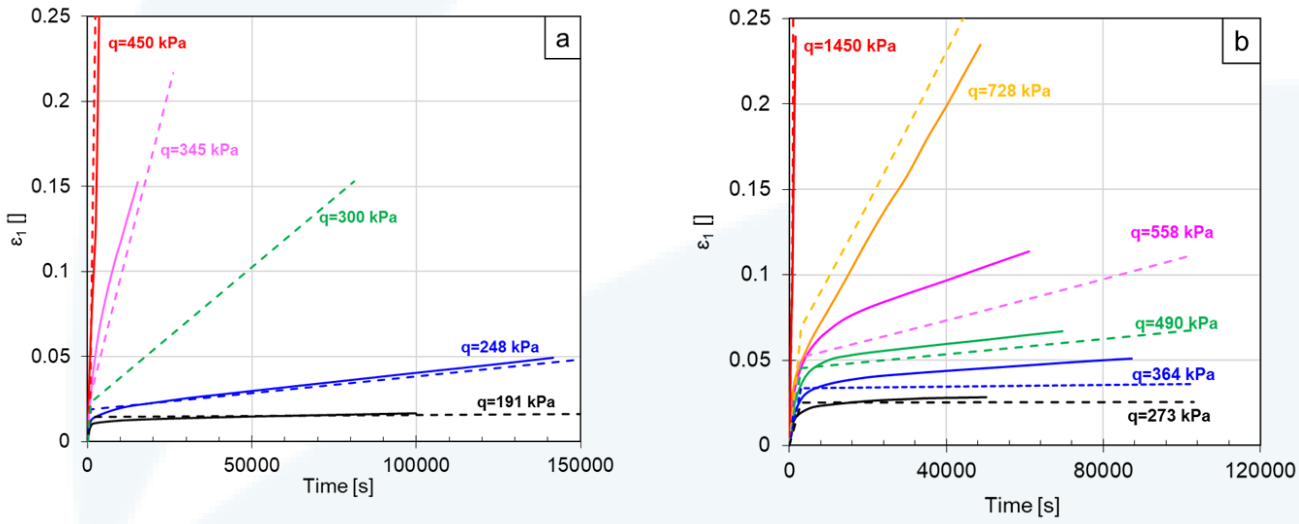

Figure 21 Creep deformation vs. time at a) T=-3 ℃, b) T=-5 ℃ (Lyu, 2021)

Table 5 Calibrated parameters for the Longyearbyen case study (Lyu, 2021)

Parameter	Description	Units	Value
	Sand 1 ($z = 0 \sim 0.7\ m$)		
e	Void ratio	-	0.27
ρ_s	Solid density	kg/m^3	2000
k_s	Thermal conductivity of solid	$W/m/K$	1
c_s	Thermal capacity of solid	$J/kg/K$	1250
	Sand 2 ($z = 0.7 \sim 3\ m$)		
e	Void ratio	-	0.351
ρ_s	Solid density	kg/m^3	2700
k_s	Thermal conductivity of solid	$W/m/K$	4
c_s	Thermal capacity of solid	$J/kg/K$	1250
	Marine clay ($z = 3 \sim 30\ m$)		
e	Void ratio	-	0.621
ρ_s	Solid density	kg/m^3	2700
k_s	Thermal conductivity of solid	$W/m/K$	2.6
c_s	Thermal capacity of solid	$J/kg/K$	1250
E_{fRef}	Frozen Soil Young's modulus at T=273.16 K	Pa	1E6
E_{flncr}	Rate of change in Young's modulus with temperature	Pa/K	1E6
ν_f	Frozen Soil Poisson's ratio	-	0.47
G_0	Unfrozen soil shear modulus	Pa	5E6
κ_0	Unfrozen soil elastic compressibility coefficient	-	0.01
p_0^*	Reference stress	Pa	-10000
λ_0	Elastic-plastic compressibility coefficient for unfrozen state	-	0.05
m	Shape parameter	-	1
γ	Plastic potential parameter	-	1
k_{t1}	Rate of change in apparent cohesion with suction	-	0.11
M	Slope of the critical state line	-	1.2
r	Coefficient related to the maximum soil stiffness	-	0.1
β	Rate of change in soil stiffness with suction	Pa^{-1}	5E-8
k_{t2}	Hardening parameter for apparent cohesion	-	0
μ_0	Fluidity parameter for unfrozen state	s^{-1}	5E-9
N_0	Rate dependency parameter for unfrozen state	-	20
b_1	Rate of change in N with suction	Pa^{-1}	3E-6
b_2	Rate of change in N with ice saturation	-	72
p_{y0r}^*	Initial equivalent stress for unfrozen state	Pa	-40000

The model is used to simulate the ground temperature variation in the NGT site at Svalbard. As mentioned, the NGTS project has recorded the ground temperature profile down to 30 *m* depth in a borehole in the site at Svalbard. The simulation is conducted for a period between 2017/09/01 to 2021/03/01. The recorded ground surface temperature history is imposed as the upper boundary (the surface) condition. The bottom boundary is closed but subjected to the geothermal heat flux 65 *mW/m2* as suggested by *Etzelmüller et al.* (2011). The initial

condition of the model is set according to the recorded temperature profile at 2017/09/01. Figure 22 compares the recorded and simulated ground temperatures at end of spring, summer and fall 2020, and late winter 2021. The overall agreement is very good, even near the surface where the monthly and daily environmental conditions by nature are large.

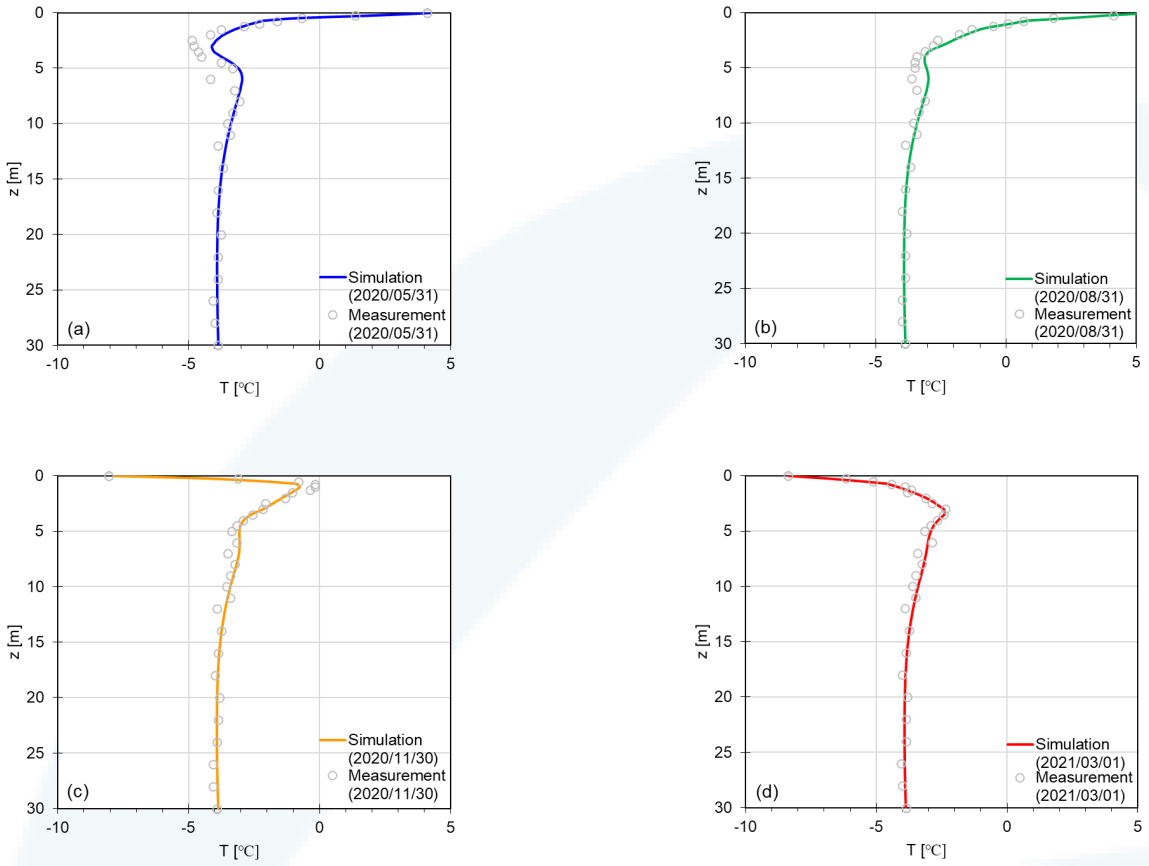

Figure 22 Measured field ground temperature profiles and numerical simulation results at end of spring 2020, summer 2020, fall 2020 and winter 2021 (Lyu, 2021)

As a part of the Nunataryuk project, a field footing test has been conducted in the NGT site at Svalbard (with similar soil layers calibrated in Table 5 and Figures 20 and 21) in order to measure and characterized the long-term (10 years) settlement of the footing in a changing climate with thawing permafrost (see (*Lyu*, 2021) for further details of the test). The results of this test are supposed to be used for the validation of the model. However, at the time of this report, the results were not ready for this purpose. We should also note that the mechanical part of the model described in this report was previously validated against field data by *Ghoreishian Amiri and Grimstad* (2017). Thus, in the rest of this section, we will continue by simulating the above-mentioned footing test and predicting the long-term (50 years) settlements of the footing without a quantitative validation with the experiment. The quantitative validation of the model with the field measurements of this test will come in upcoming publications.

The geometry of the model and the soil stratigraphy is given in Figure 23. The model domain is 30 *m* × 10 *m*, and a uniform stress (p_L) with 0.25 *m* radius is imposed on the FG boundary. The air temperature until the year 2070 follows the future climate change scenarios in the Svalbard area estimated by *Hanssen-Bauer et al.* (2019). An empirical quadratic correlation is considered from the time serial data between air temperature and ground surface temperature during 2017-2021. This relation was assumed to be generally valid for next 50 years. The estimated future ground surface temperature is imposed on the upper boundary (AC). The bottom boundary (ED)

is subjected to the geothermal heat flux 65 *mW/m2*. Different load level (p_L= 300, 450, 600 and 900 *kPa*) and footing depth (4, 6 and 8 *m*) are assumed in the simulations, and the resulted settlements has been calculated.

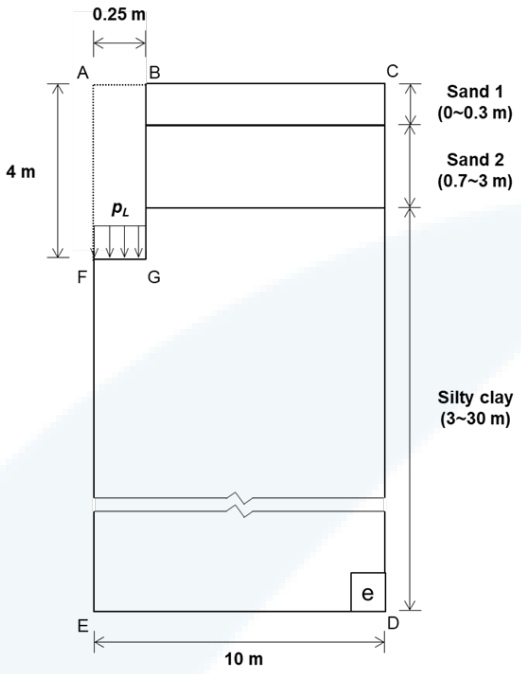

Figure 23 Geometry of the model and the soil stratigraphy for the Svalbard field footing test

The ground temperature directly influences the mechanical strength and creep behaviour of permafrost. Therefore, the evolution of ground temperature at the depth of footing (4, 6 and 8 *m*) is presented in Figure 24 according to different warming scenarios. Ground temperature at shallower depth (e.g. 4 *m*) is warmer, rises/thaws faster and shows greater fluctuation in one year compared with 6 *m* and 8 *m*. The permafrost down to 4~8 *m* would be thawed around 2045~2055 according to RCP85 vs. 2050~2065 for RCP45. The top 4 *m* of the permafrost would become active layer around 2062 while 6 *m* and 8 *m* permafrost remain frozen before 2070 for the scenario of RCP26.

The settlement rate of the footing depends on the warming scenarios, applied stress, and embedment depth as shown in Figure 25. It can be generally categorized to three phases: Phase Ⅰ: instant settlement at the start of the loading, Phase Ⅱ: steady settlement characterized as little or quite mild rate, Phase Ⅲ: accelerated settlement. The time for the transition from Phase Ⅱ to Phase Ⅲ is highly impacted by footing embedment depth and warming scenarios. In other words, the service time of footing or foundation becomes significantly shorter when shallower footing is subject to warmer scenarios. The influence of warming temperature on infrastructure settlement would become more visible after the next 10~15 years, and the subsequent significant increase of the settlement rate is a kind of early warning for infrastructure instability. It is also found that shallower footing gives stepwise settlement in one-year period (at 4 *m* vs. 6 *m* and 8 *m* in Figure 25) because of higher ground temperature fluctuation. This stepwise settlement mode has been observed by several long-term field investigations, e.g. (*Zhang et al.*, 2017).

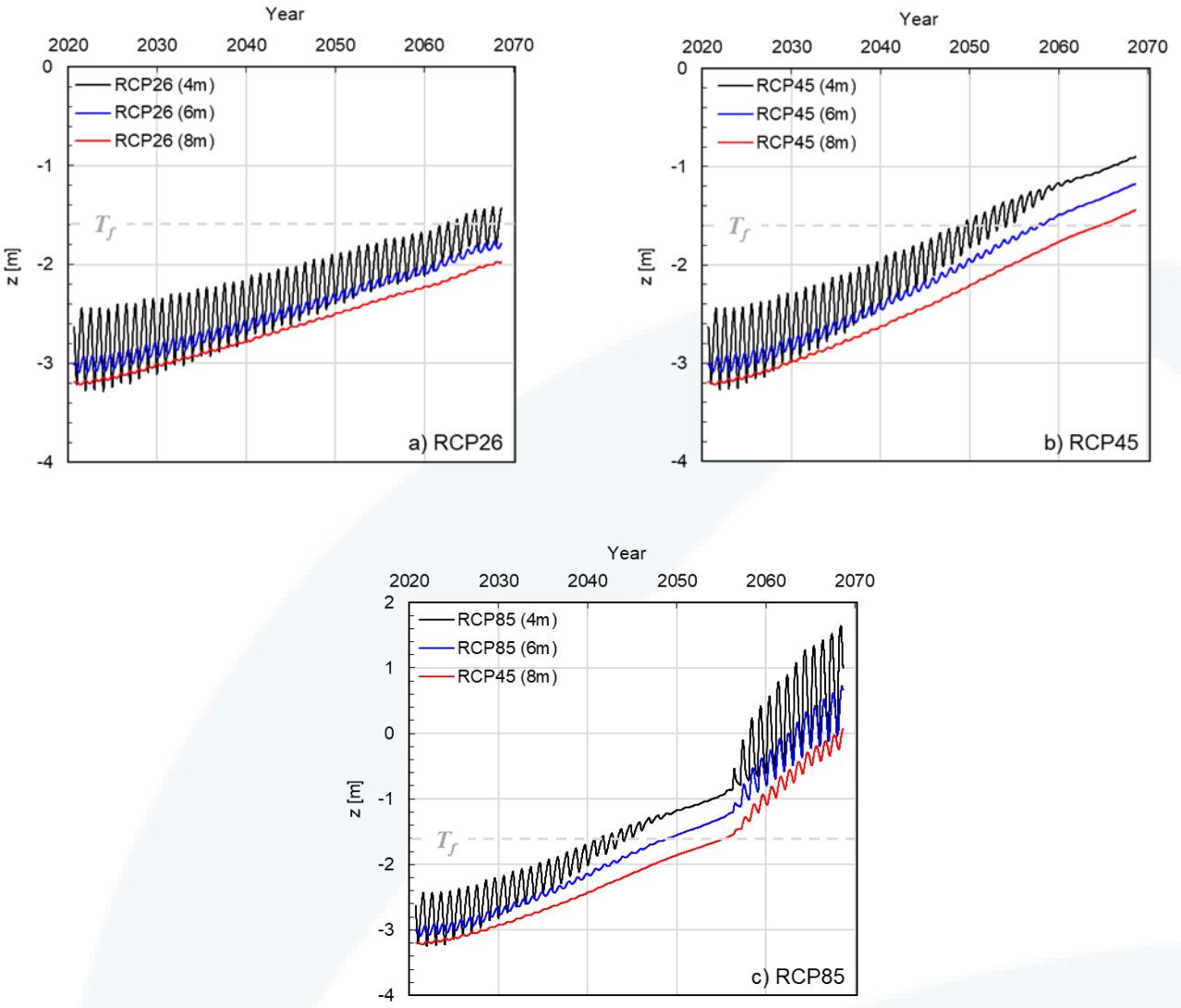

Figure 24 Ground temperature variation until the year 2070 at the depth z=4 m, 6 m, and 8 m according to different climate change scenarios: a) RCP26, b) RCP45, c) RCP85 (Lyu, 2021)

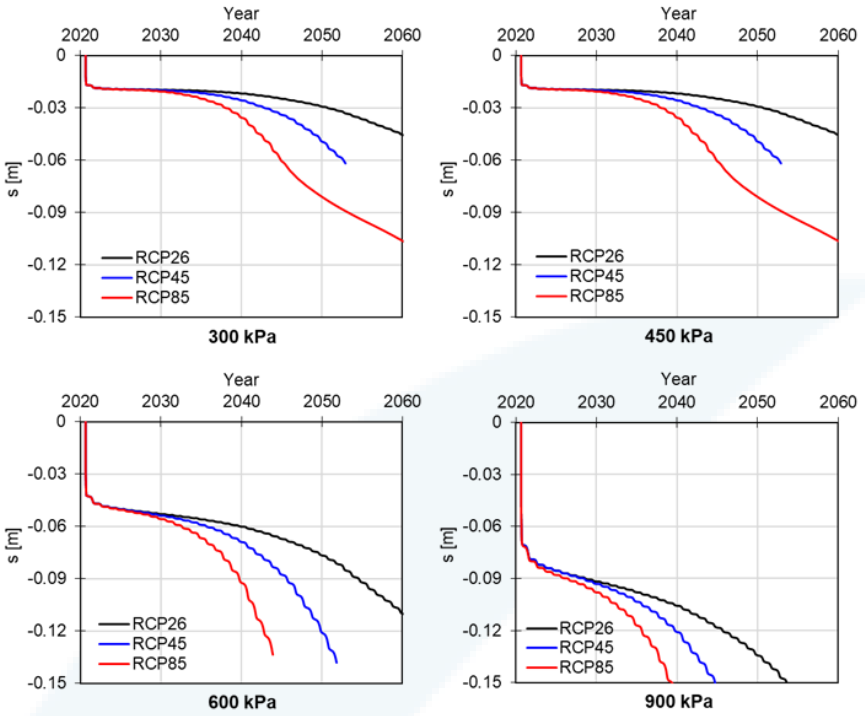
Year
2020
2030
2040
2050
2060
0
-0.03
-0.06
-0.09
-0.12
-0.15
s [m]
RCP26
RCP45
RCP85
300 kPa
450 kPa
600 kPa
900 kPa

a) z=4 m

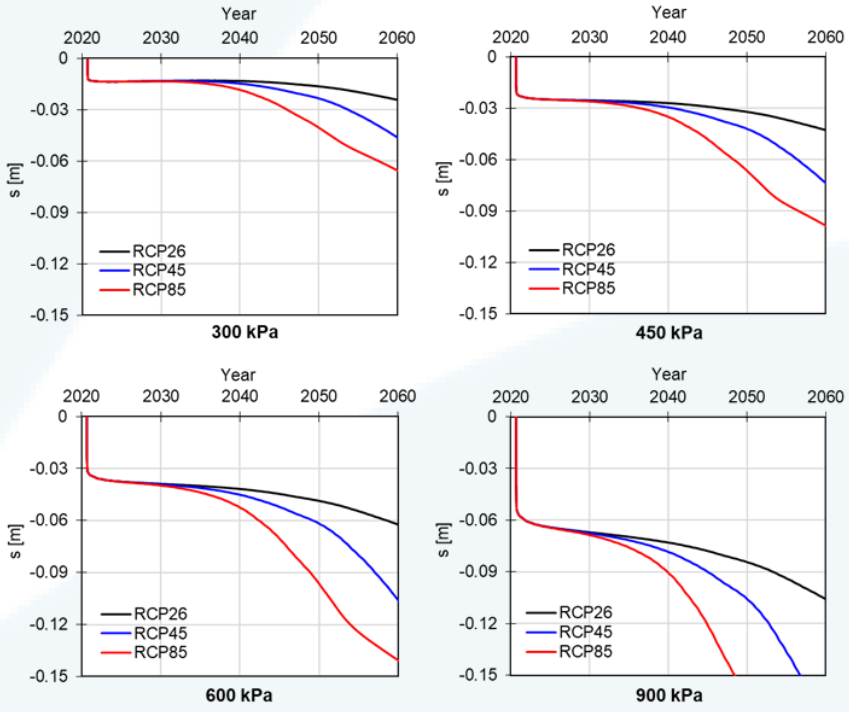
Year
2020
2030
2040
2050
2060
0
-0.03
-0.06
-0.09
-0.12
-0.15
s [m]
RCP26
RCP45
RCP85
300 kPa
450 kPa
600 kPa
900 kPa

b) z=6 m

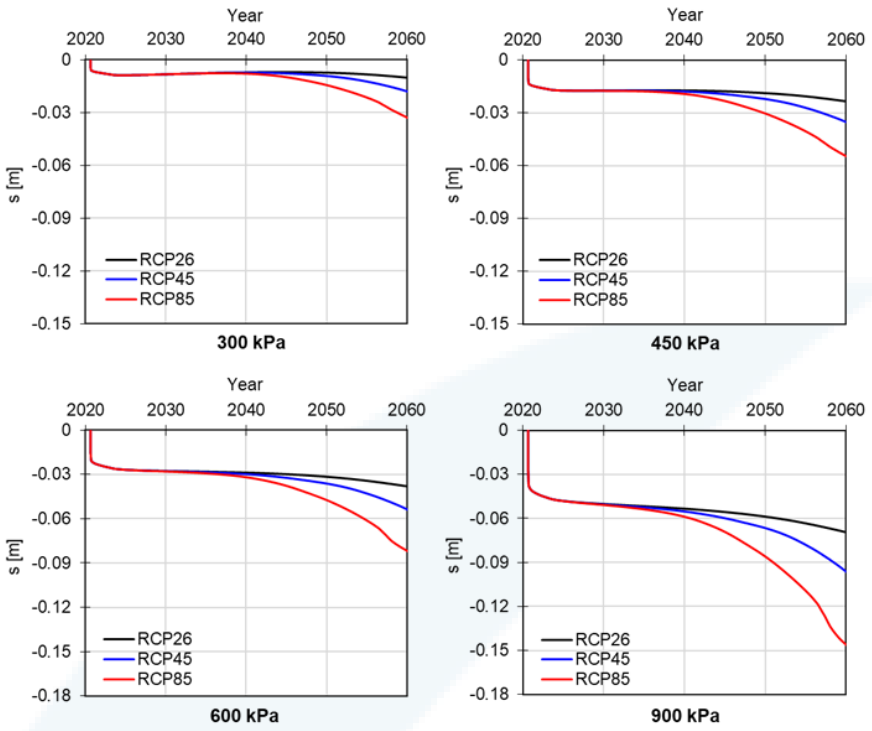

c) z=8 m

Figure 25 Footing settlement at the embedment depth z=4 m, 6 m, and 8 m with different applied load (p_L = 300, 450, 600 and 900 kPa) at z= a)4 m, b)6 m, c)8 m (Lyu, 2021)

5 References

Aré, F. E. (1988), Thermal abrasion of sea coasts (part i), *Polar Geography and Geology*, *12*(1), 1-1.

Barnhart, K. R., R. S. Anderson, I. Overeem, C. Wobus, G. D. Clow, and F. E. Urban (2014), Modeling erosion of ice-rich permafrost bluffs along the alaskan beaufort sea coast, *Journal of Geophysical Research: Earth Surface*, *119*(5), 1155-1179.

Dean, R. G., and R. A. Dalrymple (1991), *Water wave mechanics for engineers and scientists*, 368 pp., WORLD SCIENTIFIC.

Deltares (2022), *Xbeach*, https://oss.deltares.nl/web/xbeach/release-and-source.

Etzelmüller, B., T. V. Schuler, K. Isaksen, H. H. Christiansen, H. Farbrot, and R. Benestad (2011), Modeling the temperature evolution of svalbard permafrost during the 20th and 21st century, *The Cryosphere*, *5*(1), 67-79.

Ghoreishian Amiri, S. A., and G. Grimstad (2017), Constitutive model for long-term behavior of saturated frozen soil, in *Poromechanics vi*, edited, pp. 1005-1012.

Ghoreishian Amiri, S. A., G. Grimstad, and M. Kadivar (2022), An elastic-viscoplastic model for saturated frozen soils, *European Journal of Environmental and Civil Engineering*, *26*(7), 2537-2553.

Ghoreishian Amiri, S. A., G. Grimstad, M. Kadivar, and S. Nordal (2016), Constitutive model for rate-independent behavior of saturated frozen soils, *Canadian Geotechnical Journal*, *53*(10), 1646-1657.

Gilbert, G. L., H. B. O'Neill, W. Nemec, C. Thiel, H. H. Christiansen, and J.-P. Buylaert (2018), Late quaternary sedimentation and permafrost development in a svalbard fjord-valley, norwegian high arctic, *Sedimentology*, *65*(7), 2531-2558.

Graham, L. G., I. Arne, O. S. Anatoly, and A. Arne (2019), Characterization of two sites for geotechnical testing in permafrost: Longyearbyen, svalbard, *AIMS Geosciences*, *5*(4), 868-885.

Hanssen-Bauer, I., E. Førland, H. Hisdal, S. Mayer, and A. Sorteberg (2019), Climate in svalbard 2100, NCCS Report.

Hoque, M. A., and W. H. Pollard (2009), Arctic coastal retreat through block failure, *Canadian Geotechnical Journal*, *46*(10), 1103-1115.

Isaev, V. S., A. V. Koshurnikov, A. Pogorelov, R. M. Amangurov, O. Podchasov, D. O. Sergeev, S. N. Buldovich, D. M. Aleksyutina, E. A. Grishakina, and A. Kioka (2019), Cliff retreat of permafrost coast in south-west baydaratskaya bay, kara sea, during 2005–2016, *Permafrost and Periglacial Processes*, *30*(1), 35-47.

Islam, M. A., and R. Lubbad (2022), A process-based model for arctic coastal erosion driven by thermodenudation and thermoabrasion combined and including nearshore morphodynamics, *Article submitted to the Journal of Marine Science and Engineering*.

Jones, B. M., C. D. Arp, M. T. Jorgenson, K. M. Hinkel, J. A. Schmutz, and P. L. Flint (2009), Increase in the rate and uniformity of coastline erosion in arctic alaska, *Geophysical Research Letters*, *36*(3).

Jones, B. M., et al. (2020), Arctic report card 2020: Coastal permafrost erosion.

Kobayashi, N. (1985), Formation of thermoerosional niches into frozen bluffs due to storm surges on the beaufort sea coast, *Journal of Geophysical Research: Oceans*, *90*(C6), 11983-11988.

Kobayashi, N., J. C. Vidrine, R. B. Nairn, and S. M. Soloman (1999), Erosion of frozen cliffs due to storm surge on beaufort sea coast, *Journal of Coastal Research*, *15*(2), 332-344.

Lantuit, H., et al. (2011), The arctic coastal dynamics database: A new classification scheme and statistics on arctic permafrost coastlines, *Estuaries and Coasts*, *35*, 383-400.

Longuet-Higgins, M. S. (1970), Longshore currents generated by obliquely incident sea waves: 1, *Journal of Geophysical Research (1896-1977)*, *75*(33), 6778-6789.

Lyu, C. (2021), Mechanical behavior of frozen saline clay: Laboratory, field and numerical investigation, PhD Dissertation, Norwegian University of Science and Technology (NTNU).

Ramage, J., L. Jungsberg, S. Wang, S. Westermann, H. Lantuit, and T. Heleniak (2021), Population living on permafrost in the arctic, *Population and Environment*, *43*(1), 22-38.

Ravens, T. M., B. M. Jones, J. Zhang, C. D. Arp, and J. A. Schmutz (2012), Process-based coastal erosion modeling for drew point (north slope, alaska), *Journal of Waterway, Port, Coastal and Ocean Engineering*, *138*(2), 122-130.

Ravens, T. M., M. Ulmgren, M. Wilber, G. Hailu, and J. Peng (2017), Arctic-capable coastal geomorphic change modeling with application to barter island, alaska, *OCEANS 2017 – Anchorage*, 1-4.

Steele, M., W. Ermold, and J. Zhang (2008), Arctic ocean surface warming trends over the past 100 years, *Geophysical Research Letters*, *35*(2).

TU-Delft (2021), *Swan: Simulating waves nearshore.*, https://swanmodel.sourceforge.io/.

Watanabe, K., and Y. Osada (2016), Comparison of hydraulic conductivity in frozen saturated and unfrozen unsaturated soils, *Vadose Zone Journal*, *15*(5).

Zhang, H., J. Zhang, K. Zhang, and B. Zheng (2017), Long-term plate load tests in permafrost region on the qinghai-tibetan plateau, *Cold Regions Science and Technology*, *143*, 105-111.